

AD-A089 714

SCIENCE APPLICATIONS INC VIENNA VA

F/G 7/4

SOFT X-RAY PHOTOEMISSION: DEVELOPMENT OF USER ORIENTED CODE SXR--ETC(U)

MAR 80 D J STRICKLAND, D L LIN

DNA001-79-C-0084

UNCLASSIFIED

SAI-102-80-001

DNA-5307F

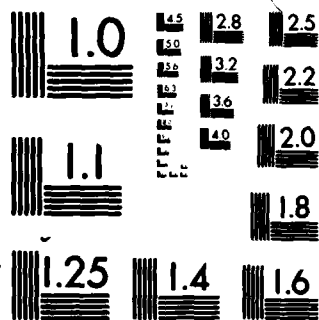
NL

END

DATE

1-1-80

DTIC



MICROCOPY RESOLUTION TEST CHART  
NATIONAL BUREAU OF STANDARDS-1963-A

**(12) LEVEL II**  
B.S.

**DNA 5307F**

**AD A089714**

**SOFT X-RAY PHOTOEMISSION: DEVELOPMENT  
OF USER ORIENTED CODE SXRP AND ITS  
APPLICATION TO PHOTOEMISSION, ELECTRON  
BACKSCATTER, CHARGE DEPOSITION AND  
ENERGY DEPOSITION**

**D. J. Strickland  
D. L. Lin  
Science Applications, Inc.  
8330 Old Courthouse Road, Suite 510  
Vienna, Virginia 22180**

**1 March 1980**

**Final Report for Period 1 November 1978—1 November 1979**

**CONTRACT No. DNA 001-79-C-0084**

**APPROVED FOR PUBLIC RELEASE;  
DISTRIBUTION UNLIMITED.**

**THIS WORK SPONSORED BY THE DEFENSE NUCLEAR AGENCY  
UNDER RDT&E RMSS CODE B323079464 R99QAXEE50118 H26000.**

**Prepared for  
Director  
DEFENSE NUCLEAR AGENCY  
Washington, D. C. 20305**

**DTIC  
ELECTE  
SEP 29 1980  
S D  
B**

**80 9 24 059**

**DOC FILE COPY**

Destroy this report when it is no longer needed. Do not return to sender.

PLEASE NOTIFY THE DEFENSE NUCLEAR AGENCY,  
ATTN: STTI, WASHINGTON, D.C. 20305, IF  
YOUR ADDRESS IS INCORRECT, IF YOU WISH TO  
BE DELETED FROM THE DISTRIBUTION LIST, OR  
IF THE ADDRESSEE IS NO LONGER EMPLOYED BY  
YOUR ORGANIZATION.



UNCLASSIFIED

SECURITY CLASSIFICATION OF THIS PAGE (When Data Entered)

REPORT DOCUMENTATION PAGE		READ INSTRUCTIONS BEFORE COMPLETING FORM
1. REPORT NUMBER DNA 5387F	2. GOVT ACCESSION NO. AD-A089 714	3. RECIPIENT'S CATALOG NUMBER 9
4. TITLE (and Subtitle) SOFT X-RAY PHOTOEMISSION: DEVELOPMENT OF USER ORIENTED CODE SXRP AND ITS APPLICATION TO PHOTO- EMISSION, ELECTRON BACKSCATTER, CHARGE DEPOSITION AND ENERGY DEPOSITION		5. TYPE OF REPORT & PERIOD COVERED Final Report, for Period 1 Nov 78-1 Nov 79
7. AUTHOR D. J. Strickland D. L. Lin	14. PERFORMING ORG. REPORT NUMBER SAI-102-80-001	6. CONTRACT OR GRANT NUMBER(s)
9. PERFORMING ORGANIZATION NAME AND ADDRESS Science Applications, Inc. 8330 Old Courthouse Road, Suite 510 Vienna, Virginia 22180	10. PROGRAM ELEMENT, PROJECT, TASK AREA & WORK UNIT NUMBERS SUBTASK R99QAXEE501-18	15. SECURITY CLASS (of this report) UNCLASSIFIED
11. CONTROLLING OFFICE NAME AND ADDRESS Director Defense Nuclear Agency Washington, D.C. 20305	12. REPORT DATE 1 March 1980	13. NUMBER OF PAGES 66
14. MONITORING AGENCY NAME & ADDRESS (if different from Controlling Office) 627015	15a. DECLASSIFICATION/DOWNGRADING SCHEDULE	
16. DISTRIBUTION STATEMENT (of this Report)  Approved for public release; distribution unlimited.		
17. DISTRIBUTION STATEMENT (of the abstract entered in Block 20, if different from Report)		
18. SUPPLEMENTARY NOTES  This work sponsored by the Defense Nuclear Agency under RDT&E RMSS Code B323079464 R99QAXEE50118 H2590D.		
19. KEY WORDS (Continue on reverse side if necessary and identify by block number)  Soft X-ray Photoemission SGEMP		
20. ABSTRACT (Continue on reverse side if necessary and identify by block number)  This work is a continuation of our program to characterize soft X-ray photo- emission for various materials used in space systems. The code SXRP is developed specifically to achieve this goal. Results predicted by this code for X-ray line sources are compared with measurements in this report. General agreement is found between theory and experiments. To assist SGEMP analysts in modeling the electromagnetic environment of systems exposed to soft X-ray in simulation test, a user-oriented algorithm for choosing transport energy		

DD FORM 1 JAN 73 1473

EDITION OF 1 NOV 65 IS OBSOLETE

UNCLASSIFIED

SECURITY CLASSIFICATION OF THIS PAGE (When Data Entered)

411539

JCB

UNCLASSIFIED

SECURITY CLASSIFICATION OF THIS PAGE(When Data Entered)

20. ABSTRACT (Continued)

grid is successfully developed for code SGRP. Electron backscatter of Al and Au are investigated to further test the scattering model in code SGRP. Another investigation concerned charge and energy deposition in Teflon for incident soft electron sources. Both investigations demonstrate the capability of SGRP to treat external electron as well as X-ray sources.

UNCLASSIFIED

SECURITY CLASSIFICATION OF THIS PAGE(When Data Entered)

## TABLE OF CONTENTS

	<u>PAGE</u>
SECTION 1: INTRODUCTION AND SUMMARY .....	5
SECTION 2: FURTHER CHARACTERIZATION OF SOFT X-RAY PHOTOEMISSION — EMISSION FOR LINE SOURCES .....	8
SECTION 3: INCORPORATING A SELF-CONTAINED ENERGY GRID SELECTION SCHEME INTO CODE SXRP .....	28
SECTION 4: ADDITIONAL STUDIES DOCUMENTED IN PUBLICATIONS .....	38
REFERENCES .....	40
APPENDIX A: ELECTRON TRANSPORT PROPERTIES FOR SOFT ELECTRON SOURCES INCIDENT ON CONDUCTING AND INSULATING MATERIALS.	
APPENDIX B: PHOTOEMISSION FROM Ag AND C FOR AN EXPLODING WIRE RADIATOR SOURCE .	
APPENDIX C: PHOTOIONIZATION CROSS SECTIONS, ELECTRON-IMPACT INVERSE MEAN FREE PATHS, AND STOPPING POWERS FOR EACH SUBSHELL OF SILVER .	

## LIST OF FIGURES

	<u>PAGE</u>
FIGURE 1: Primary yield for Al in electrons/photon versus photon energy in keV. BS refers to the measurements of Bernstein and Smith. Dashed curves come from empirical models. See discussion on page 11.....	13 12
FIGURE 2: Primary yield for aluminum oxide in electrons/photon.....	13
FIGURE 3: Primary yield for silicon dioxide in electrons/photon.....	14
FIGURE 4: Primary yield for gold in electrons/photon....	15
FIGURE 5: Primary yield for silver in electrons/photon..	16
FIGURE 6: Primary yield for carbon in electron/photon...	17
FIGURE 7: Photoemission spectrum in electrons/photon-keV and its cumulative yield in electrons/photon for a 1.49 keV Gaussian photon source incident on Al.....	20
FIGURE 8: Photoemission spectrum and its cumulative yield for a 2.64 keV Gaussian photon source incident on Al.....	21
FIGURE 9: Photoemission spectrum and its cumulative yield for a 2.64 keV Gaussian photon source incident on Al <sub>2</sub> O <sub>3</sub> .....	22
FIGURE 10: Photoemission spectrum and its cumulative yield for a 2.64 keV Gaussian photon source incident on SiO <sub>2</sub> .....	23
FIGURE 11: Photoemission spectrum and its cumulative yield for a 4.12 keV Gaussian photon source incident on Au.....	24
FIGURE 12: Photoemission spectrum and its cumulative yield for a 4.12 keV Gaussian photon source incident on Ag.....	25



# LIST OF FIGURES (CONCLUDED)

	<u>PAGE</u>
FIGURE 13: Photoemission spectrum and its cumulative yield for a 1.49 keV Gaussian photon source incident on C.....	26
FIGURE 14: Electron source spectrum for a 5.4 keV Gaussian photon source incident on Au. Dots show grid determined by grid selection scheme..	29
FIGURE 15: Electron source spectrum for a 1.49 keV Gaussian photon source incident on Ag. Dots show grid determined by grid selection scheme..	30
FIGURE 16: Photoelectron spectrum and its cumulative yield for a 5.4 keV Gaussian photon source incident on Au. Dots show grid determined by grid selection scheme.....	32
FIGURE 17: Photoelectron spectrum and its cumulative yield for a 1.49 keV Gaussian photon source incident on Ag. Dots show grid determined by grid selection scheme.....	33

ACCESSION for		
NTIS	White Section	<input checked="" type="checkbox"/>
DDC	Buff Section	<input type="checkbox"/>
UNANNOUNCED		<input type="checkbox"/>
JUSTIFICATION _____		
BY _____		
DISTRIBUTION/AVAILABILITY CODES		
Dist.	AVAIL	and/or SPECIAL
A		

## LIST OF TABLES

	<u>PAGE</u>
TABLE 1. X-RAY FLOURESCENT LINES CONSIDERED AS PHOTO-EMISSION SOURCES IN THIS WORK.....	9

## Section 1

### INTRODUCTION AND SUMMARY

This report deals with SAI's continuing program to rigorously characterize photoemission for soft X-ray sources incident on various materials found on space systems. Over the past three years, DNA has jointly sponsored the given theoretical effort<sup>1-10</sup> and an experimental one by Bernstein of ARACOR<sup>11-13</sup> to define photoemission properties for plasma radiator sources (PRS). Such information allows SGEMP analysts to model the electromagnetic environment of systems exposed to PRS radiation in simulation tests. Overall, the joint program has been a successful one. Theory has provided a detailed description of the features found in photoemission as well as a detailed description of the transport process itself. Generally good agreement has been achieved between theory and experiment in the primary photoemission yield for most materials considered. Such agreement provides confidence that photoemission is being well characterized. Where agreement has not been so satisfactory, further investigation has been carried out leading to better understanding of the given material.

PRS's do not provide as much control as one would like to have for comparing theory with experiment. Not only are there variations in the X-ray output from shot-to-shot but there are also the rapid time variations within a given shot on the scale of tens of

nanoseconds. Continuous low fluence X-ray line sources, on the other hand, in principle, provide for complete control of experimental conditions. Based on these considerations, with the desire to further test photoemission characterization from the joint program, DNA has sponsored photoemission measurements by Bernstein for X-ray line sources and predictions by us using code SXRP for the same sources. Many of these theoretical results will be presented in this report.

DNA has been the primary sponsor for development of code SXRP. This is a large code which solves the Boltzmann transport equation in matrix form derived from the integro-differential form of the equation. The solution is expressed as a flux in the variables  $z(\text{cm})$ ,  $E(\text{keV})$ , and  $\mu$  (direction cosine). The front surface solution has been of interest in this program. The code has considerable input in the form of atomic parameters and gridding information, the latter requiring modifications from run to run. Based on the difficulty in selecting good electron energy grids, one would have to say that code SXRP is not a user-oriented code. DNA has recently expressed interest, however, in having the code achieve this status based presumably on the importance attached to soft X-ray photoemission, the vigorous nature of the solution, the success in code validation, and the many material models developed to date. A significant step was made during the past year toward this goal by developing an algorithm for selecting the electron energy grid. This proved to be a difficult task due to how highly structured the photoelectron source spectrum can be and constituted a major effort during this contract

period. A description of the algorithm and a demonstration of its capability will be given in this report.

The above discussions cover most of the effort carried out under the given contract. There were, however, some additional investigations reported on at the 1979 IEEE meeting on nuclear science. One of these dealt with electron backscatter characteristics for Al and Au. This work was motivated by our desire to further critically test the scattering model in code SGRP. Another investigation concerned charge and energy deposition in Teflon for incident soft electron sources. Out of this work has come a material model for teflon and a demonstration of code SGRP's capability to treat external electron as well as X-ray sources. An examination was also made of the discrepancy between theory and experiment for PRS radiation incident on Ag. Results from these assorted studies will be found in the appendices which contain the papers as published in the IEEE journal. From recent work, we have also generated a paper in Journal of Applied Physics. A copy of this also appears in the appendices.

## Section 2

### FURTHER CHARACTERIZATION OF SOFT X-RAY PHOTOEMISSION — EMISSION FOR LINE SOURCES

In this section, photoemission properties Al, Al<sub>2</sub>O<sub>3</sub>, SiO<sub>2</sub>, Au, Ag and C will be discussed for narrow X-ray sources effectively simulating line sources. Selected results for such sources have previously appeared for Al and Au<sup>1,2,7</sup>. They were obtained shortly after the respective material models were developed to compare with available published data in the form of the primary yield (electron/photon for electron energies  $\geq 50$  eV). Here, for the six materials listed above, we will be comparing primary yields with Bernstein's measured values considering several X-ray lines between 1.26 and 5.4 keV. Table 1 lists the lines and their energies.

For a given material, results have not been obtained for all lines. We had planned to do so as well as at other energies but did not have sufficient computer time due to additional investigations related to backscatter from Al and Au and charging in Teflon. It is our desire to eventually produce a soft X-ray photoemission handbook which will contain a much more comprehensive set of results of the type to follow.

In addition to primary yields, we will also be presenting photoemission spectra for selected lines.

TABLE 1. X-RAY FLUORESCENT LINES CONSIDERED  
AS PHOTOEMISSION SOURCES IN THIS WORK

<u>EMITTER</u>	<u>h<math>\nu</math> (keV)</u>
Mg	1.26
Al	1.49
Si	1.74
Cl	2.64
Sc	4.12
Cr	5.41

Spectral comparisons with experiment, however, will not be made in this report. Bernstein has been measuring photoemission spectra and some preliminary comparisons have been made. The reporting of such information shall await his own presentation of the measurements.

It can be stated, however, that greater variations appear in the calculated spectrum which cannot be accounted for solely by differences in resolution. In particular, code SXRP gives a more rapid fall off with decreasing electron energy away from spectral maxima. This difference in behavior has also been observed with respect to a limited amount of data by Denisov et al.<sup>14</sup> (see Strickland et al.<sup>5</sup> for details). There, as here, we observe that the data agree more closely with SXRP bulk solutions. The cause of the discrepancy is not understood at this time.

We have approximated the X-ray line source by the following Gaussian distribution:

$$F(h\nu) = \exp[-(h\nu - h\nu_0)/\alpha]^2$$

where  $h\nu_0$  is the line energy and  $\alpha$  is sufficiently small that the finite extent of  $F$  has little effect on either the yield or the spectral behavior of the photoemission. Examples of source spectra will be given in the next section which illustrate the finite extent of  $F$ .

We now proceed to the results and a comparison with the measurements of Bernstein and Smith<sup>13</sup>. Comparisons with other data may be found in two previous



reports<sup>2,7</sup>. Figures 1-6 give the primary yields in electrons/photon versus photon energy for Al, Al<sub>2</sub>O<sub>3</sub>, SiO<sub>2</sub>, Au, Ag and C. The two dashed curves come from a simple empirical model<sup>15,16</sup> and are included primarily to show where absorption edges occur. The upper of the two curves implicitly includes electrons down to 10 eV while the lower one includes them down to only 100 eV. The term in the empirical formula giving the difference is the range. Burke<sup>16</sup> generated his results using 10 eV ranges and obtained favorable agreement with many sets of primary yield data. It would appear to be more appropriate, however, to use the 100 eV range since 100 eV is near the low energy cut off (by convention) for primary electron emission. This is why we include the empirical results for the 100 eV range in the figures. We note that the two curves for Au are significantly different from one another and that the more appropriate result is in poor agreement with the SXRFP results and measurements. Based on such observations, one should probably not take too seriously either good or poor agreement between the empirical model and other results, at least at the lower energies where the choice of cut off affecting the range becomes important. The model is a useful tool, however, for estimating the general behavior of the primary yield versus photon energy.

Regarding the comparison between code SXRFP's results and the measurements, we view the extent of agreement to be satisfactory considering that the calculations are done for ideally clean, smooth surfaces with pure material beneath them which can only approximate experimental conditions. In general, our yields

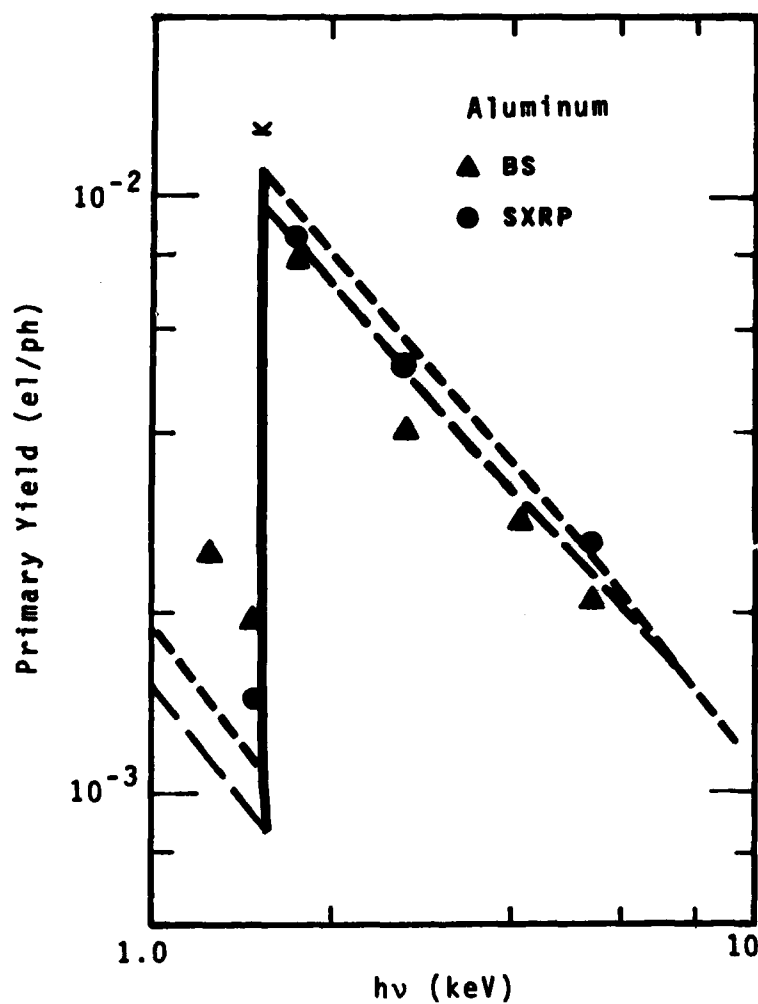


Figure 1 Primary yield for Al in electrons/photon versus photon energy in keV. BS refers to the measurements of Bernstein and Smith.<sup>13</sup> Dashed curves come from empirical models. See discussion on page 11.

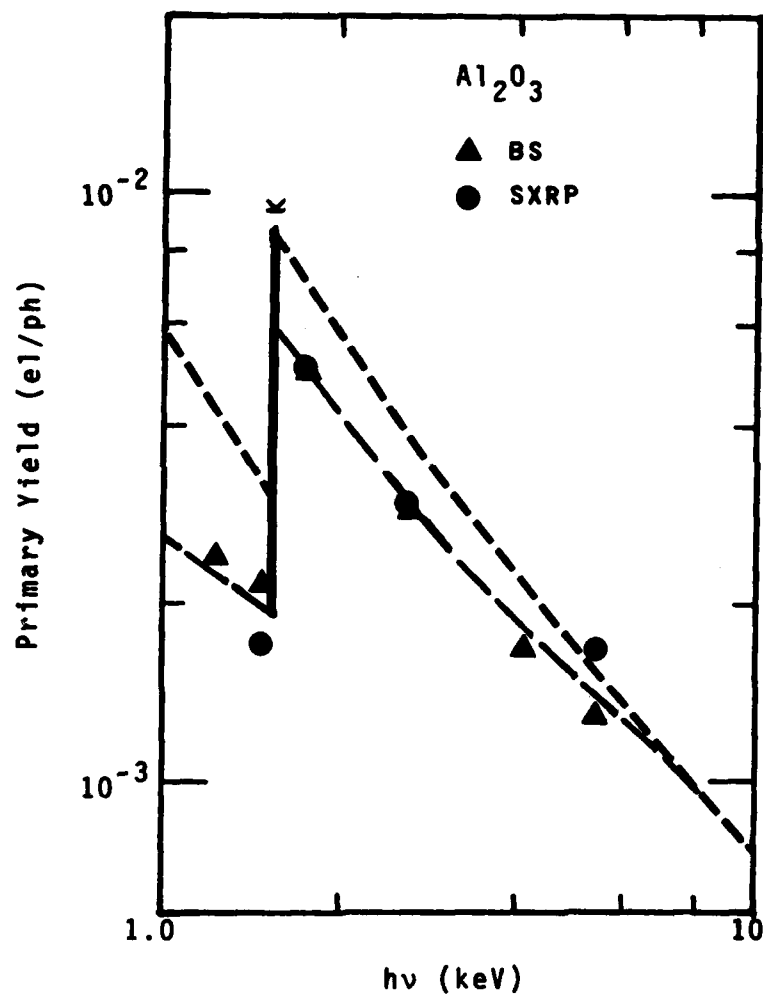


Figure 2 Primary yield for aluminum oxide in electrons/photon.

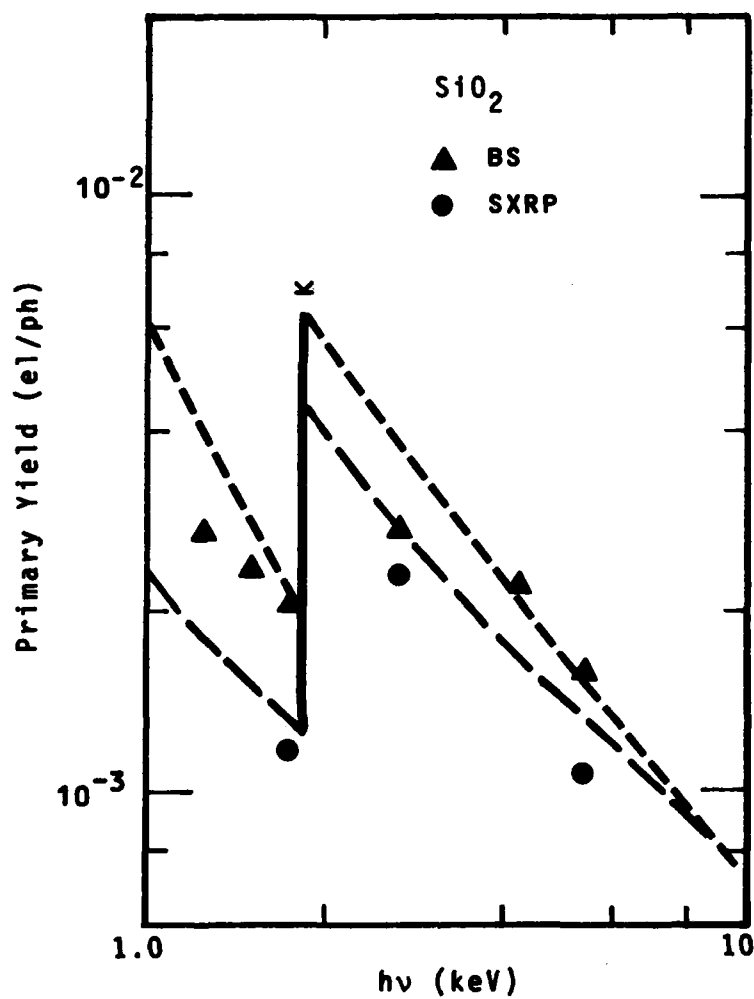


Figure 3 Primary yield for silicon dioxide in electrons/photon.

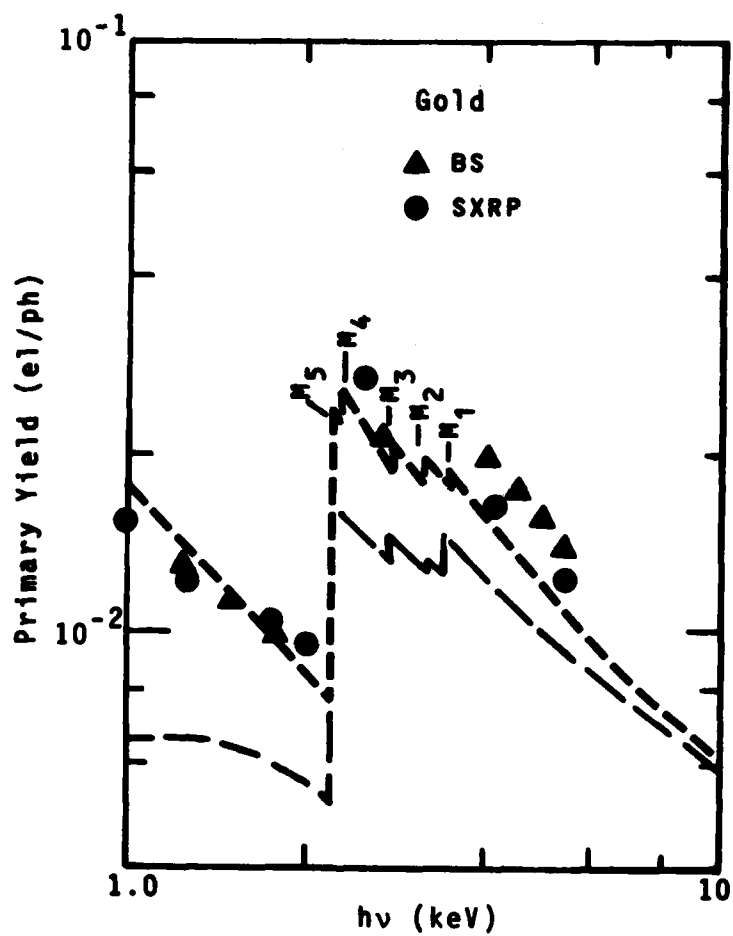


Figure 4 Primary yield for gold in electrons/photon.

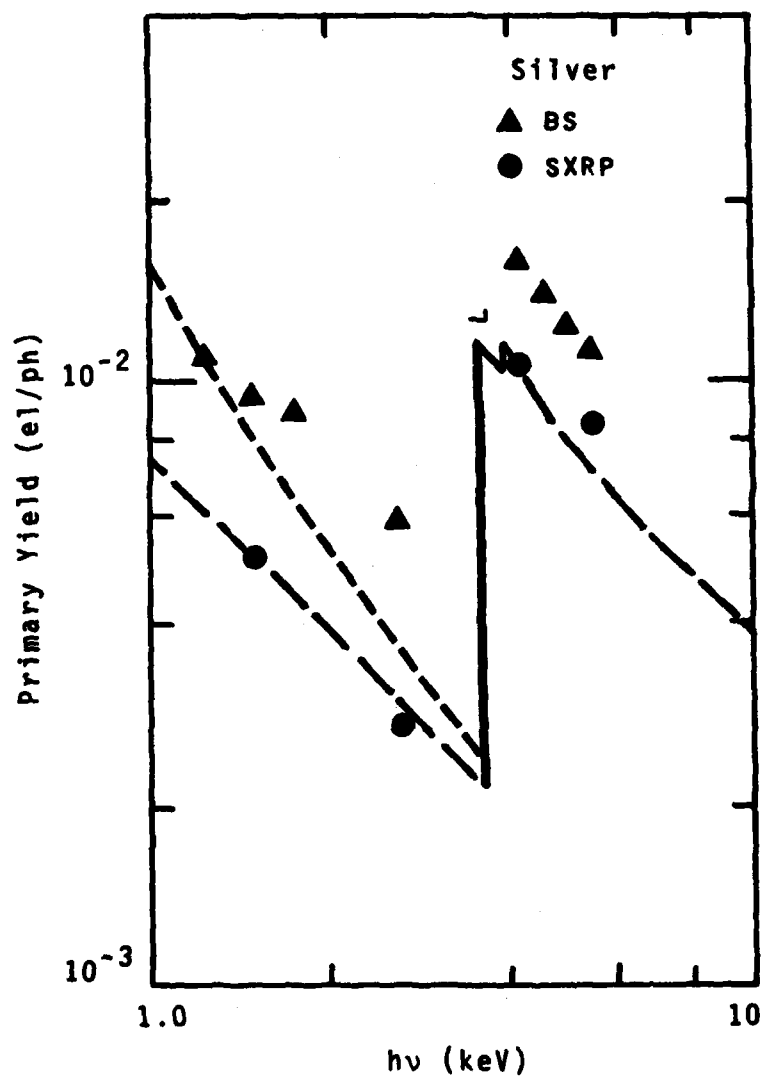


Figure 5 Primary yield for silver in electrons/photon.

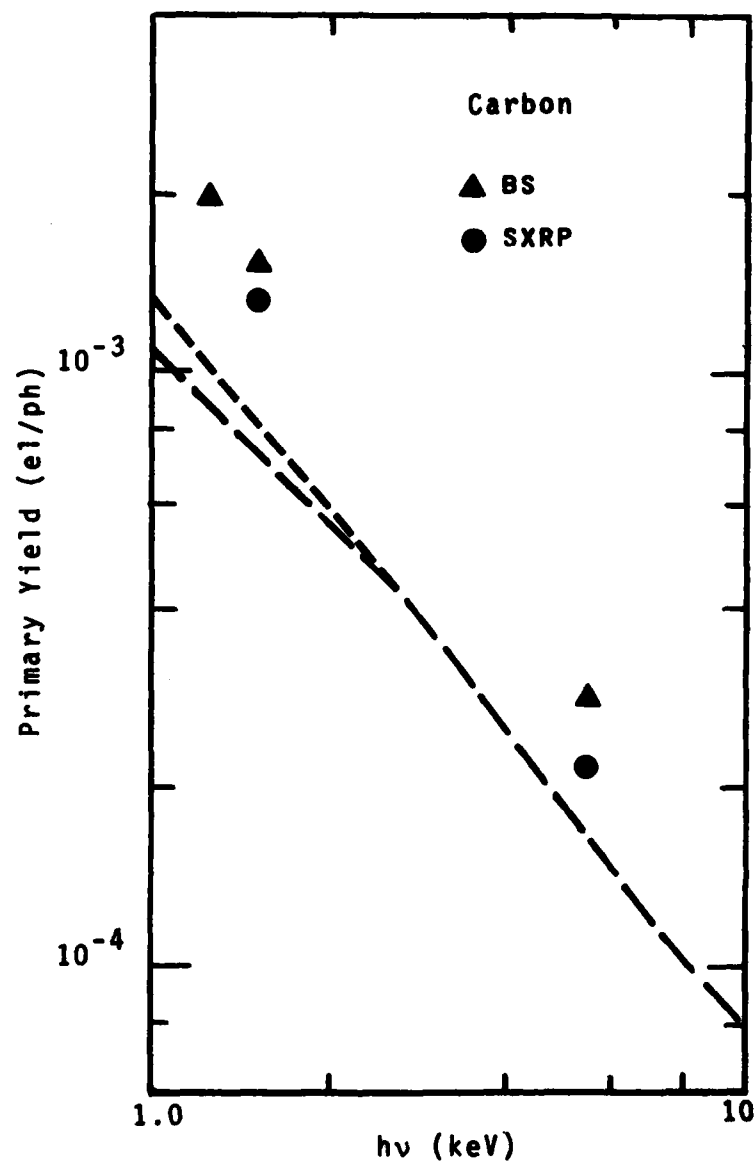


Figure 6 Primary yield for carbon in electrons/photon.

fall below the measurements but by usually less than 50% (see figures for SiO<sub>2</sub>, Au, Ag and C). Surprisingly, some of the most favorable comparisons have been made for Au which is the most difficult to model of those considered. Experimentally, however, one can approach the ideal situation (as modelled) more closely for Au than other materials such as Al which rapidly forms an oxide coating.

The largest differences are found for Ag below its L edge at  $\sim 3.5$  keV. Differences as large as a factor of two exist and happen to occur in the region dominated by the OWL II' PRS X-ray spectrum. The OWL II' source has received most of the attention both in Bernstein's and our program. Previously, direct comparisons for this source revealed about the same discrepancy noted above. The given differences have prompted us to investigate Ag in greater detail. Since good agreement had been previously achieved for Au, we decided to compare transport properties between Ag and Au by allowing for the same electron source spectrum in each material. We found, as expected, that such properties are similar. This leads one to the conclusion that differences in yield for these materials are primarily the result of differences in respective electron source spectra. Since source spectra are easy to specify, we concluded that our results for Ag should be as accurate as those for Au. Further details may be found in Appendix B which contains figures of electron source spectra and photoemission spectra used in this analysis.



We now turn our attention to spectral characteristics of photoemission. Results will follow in units of electrons/photon-keV versus electron energy for a few select line sources. The purpose of presenting such information is to illustrate the complexity which can exist in a photoemission spectrum and the diversity possible in going from one X-ray energy to another and from one material to another. Spectra will not be presented for all cases treated in this current investigation. They are available from the authors and will probably appear in a future handbook as part of a larger set of results.

The selected spectra appear in Figures 7-13. Shown in each figure are the spectrum and its corresponding cumulative yield down to  $\sim .1$  keV. The first two spectra shown (Figures 7 and 8) are for the Al K-line (1.49 keV) and Cl K-line (2.64 keV) incident on Al. These lines straddle the Al K-edge (1.56 keV) and, as can be seen, produce significantly different spectra and yields. The features are identified in each figure and are either photoelectron (single letter for shell from which electron is ejected) or Auger (three letters). The first letter in the Auger designation gives the shell from which a photoelectron is ejected. The second letter gives the shell from which an electron originates that drops into the created vacancy. The third letter gives the shell from which the Auger electron is ejected.

A demonstration of material effect on the photoemission spectrum is provided by Figure 8 for Al just discussed and Figures 9 and 10 for  $\text{Al}_2\text{O}_3$  and  $\text{SiO}_2$ , all of which refer to the Cl K-line source. Fairly

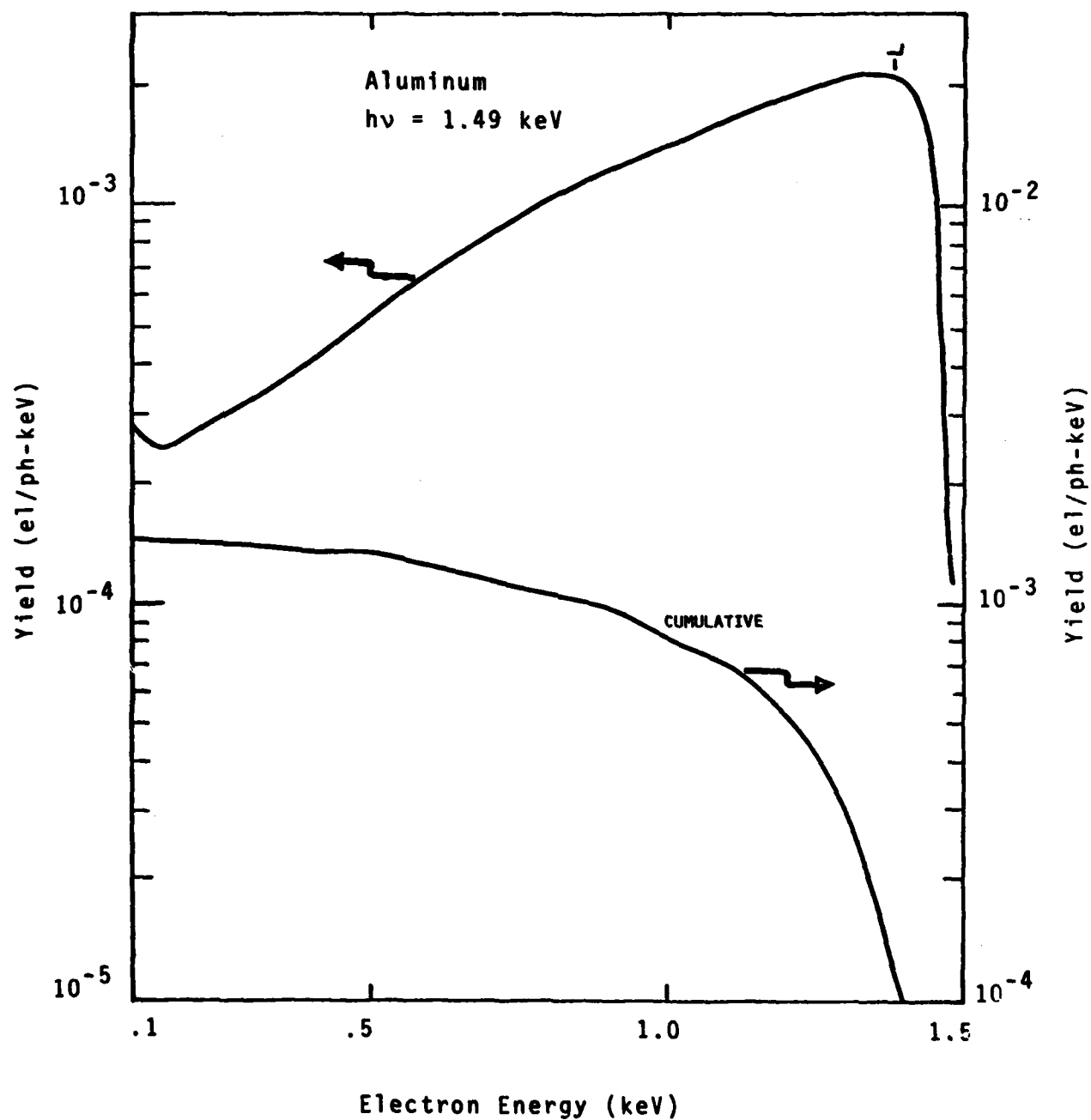


Figure 7 Photoemission spectrum in electrons/photon-keV and its cumulative yield in electrons/photon for a 1.49 keV Gaussian photon source incident on Al.

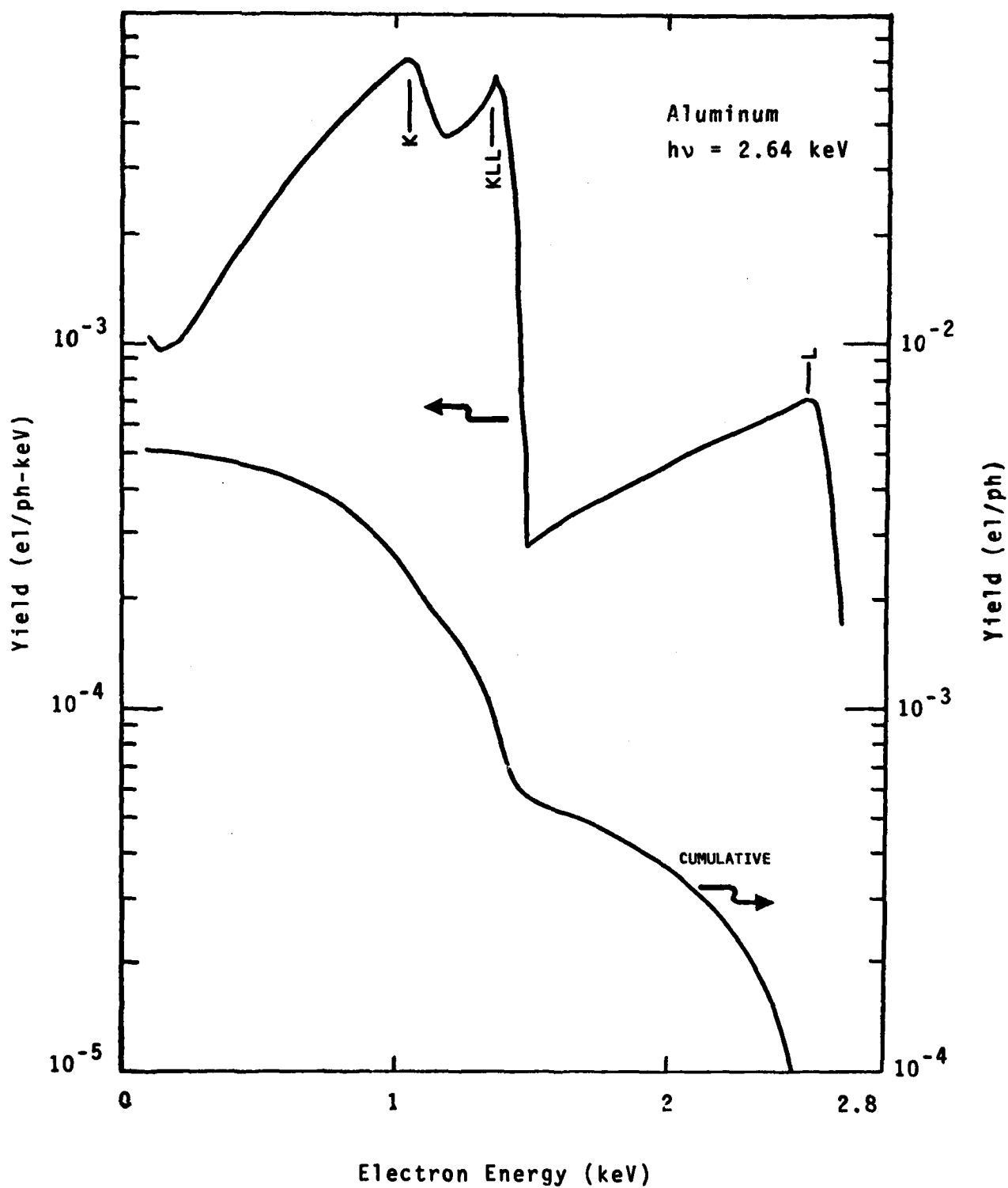


Figure 8 Photoemission spectrum and its cumulative yield for a 2.64 keV Gaussian photon source incident on Al.

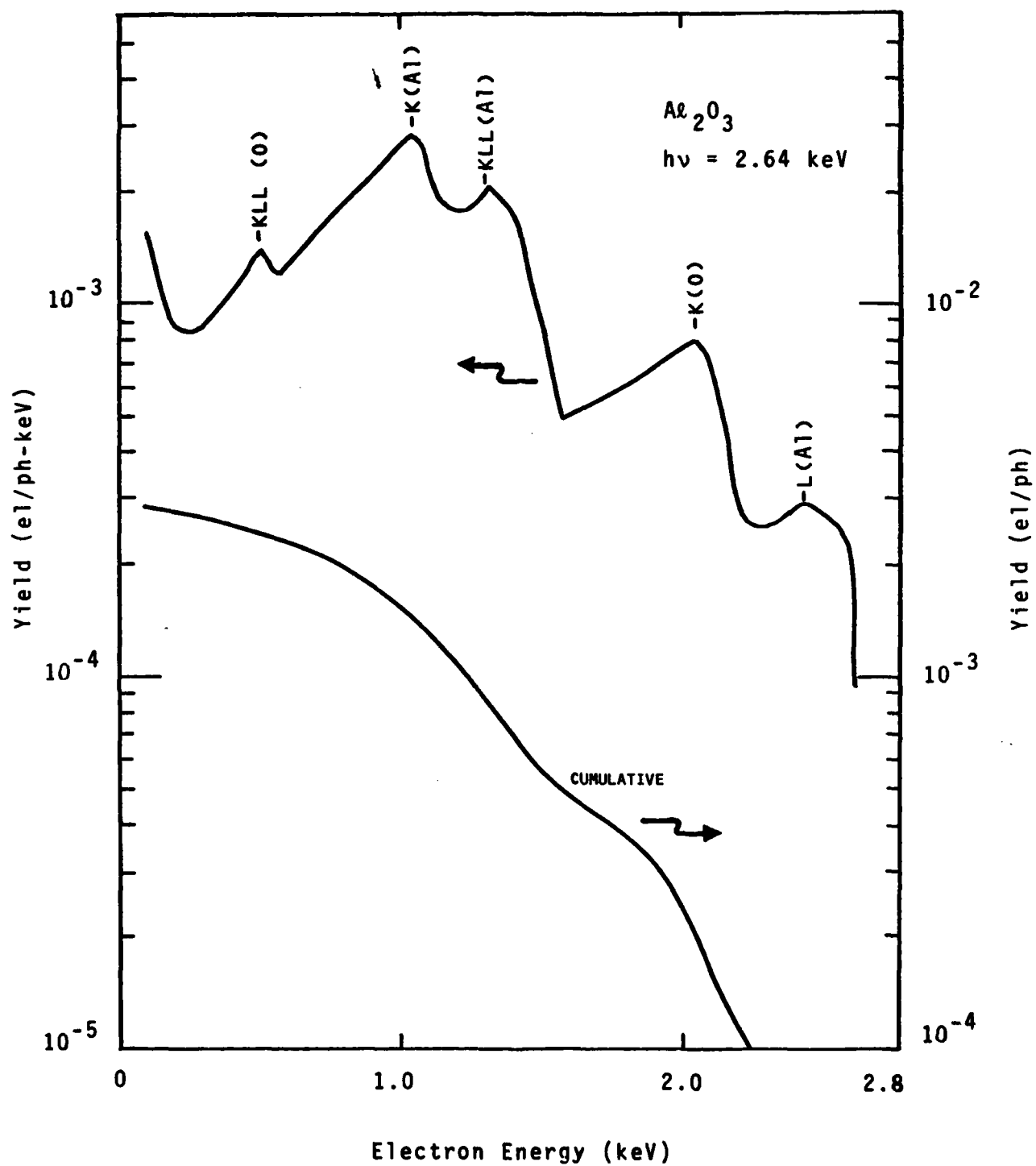


Figure 9 Photoemission spectrum and its cumulative yield for a 2.64 keV Gaussian photon source incident on  $\text{Al}_2\text{O}_3$ .

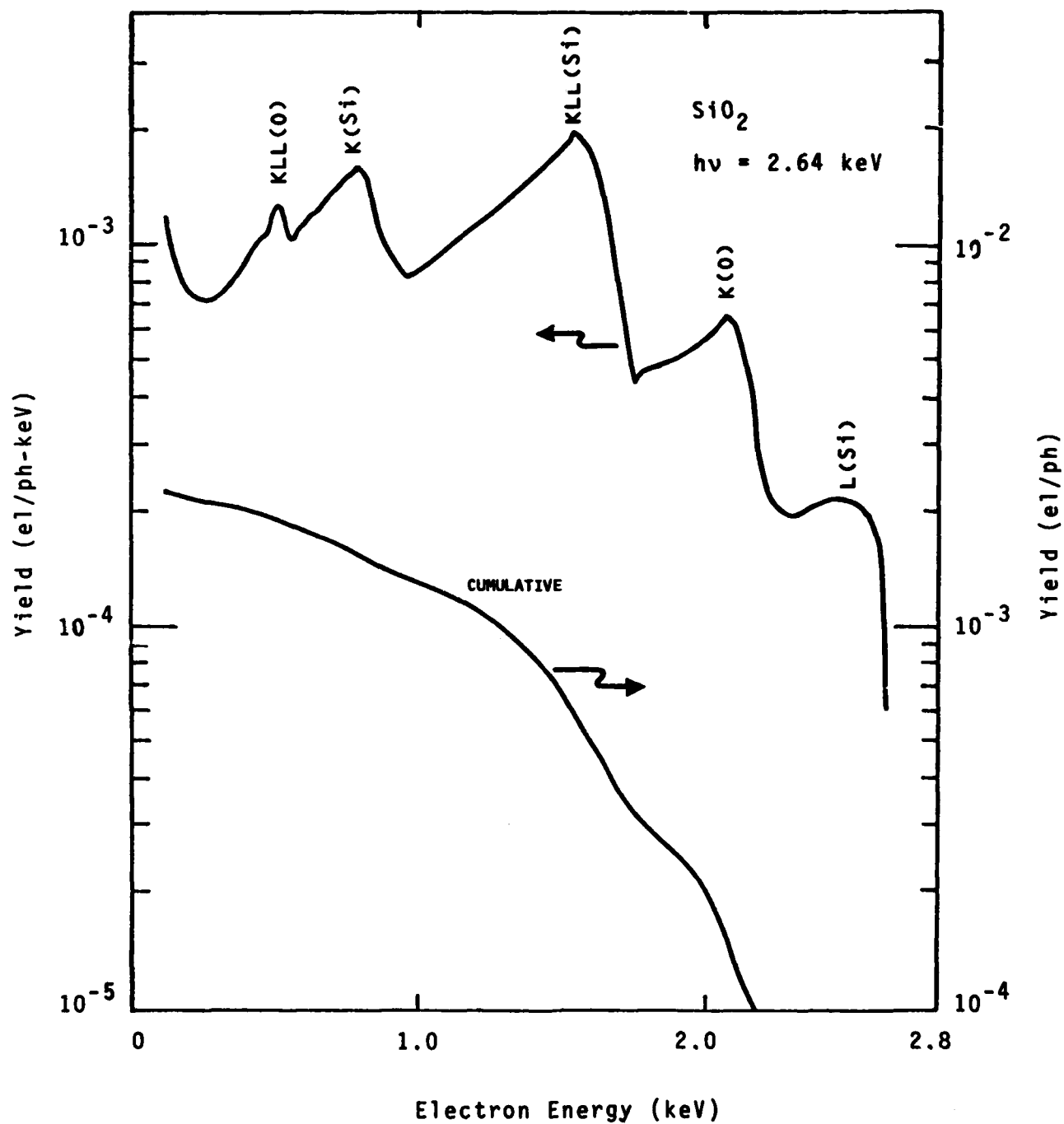


Figure 10 Photoemission spectrum and its cumulative yield for a 2.64 keV Gaussian photon source incident on  $\text{SiO}_2$ .

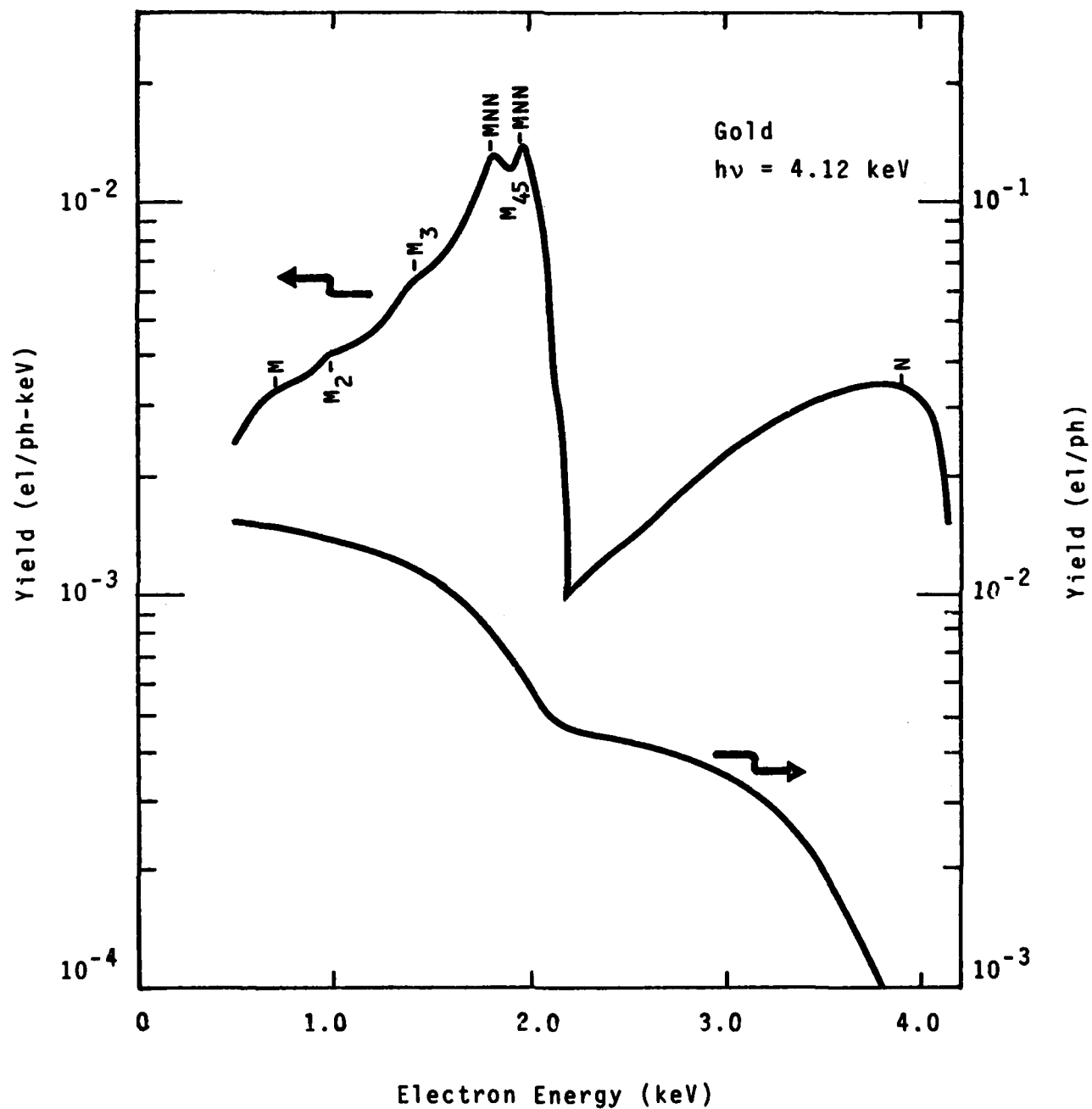


Figure 11 Photoemission spectrum and its cumulative yield for a 4.12 keV Gaussian photon source incident on Au.

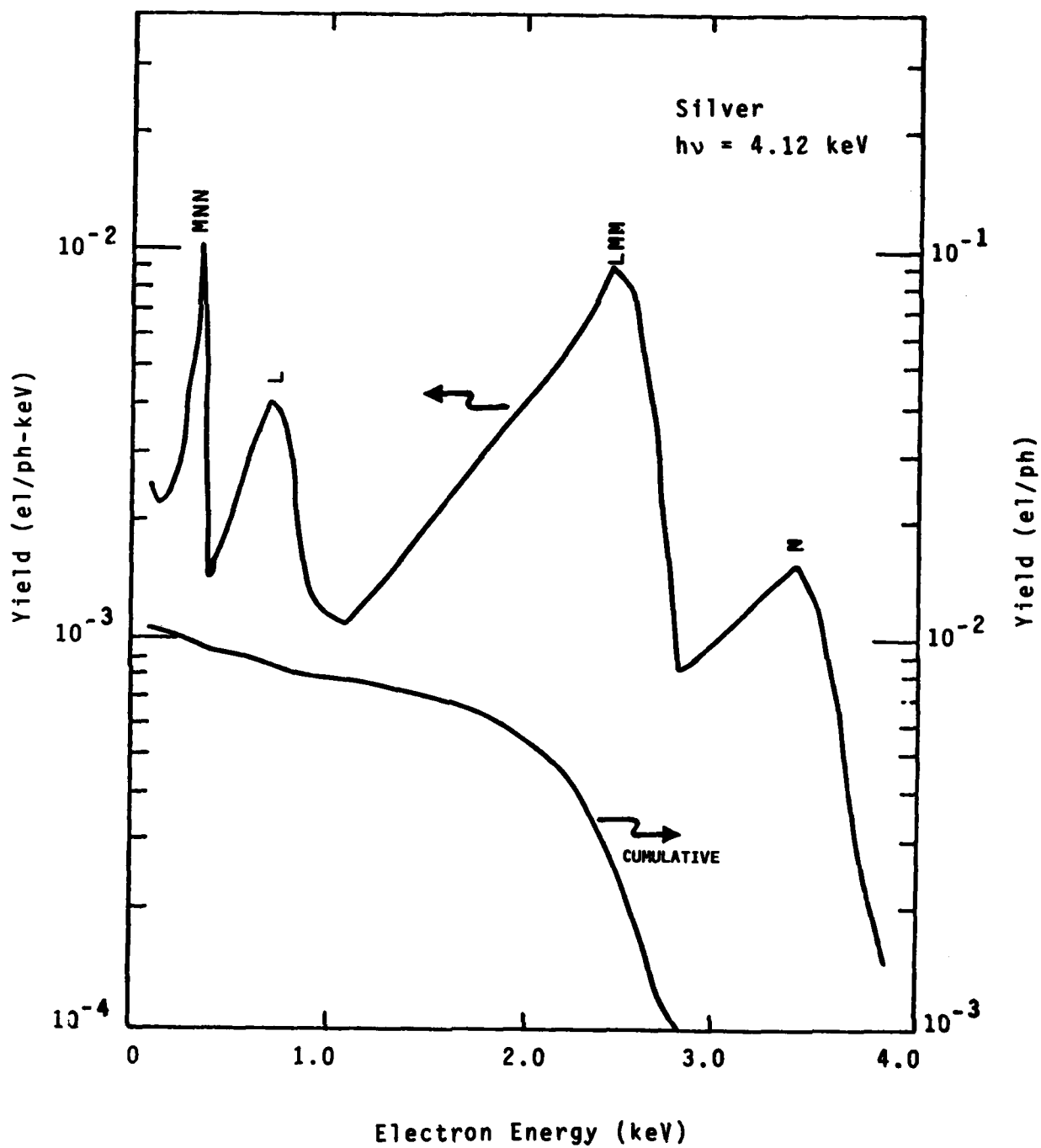


Figure 12 Photoemission spectrum and its cumulative yield for a 4.12 keV Gaussian photon source incident on Ag.

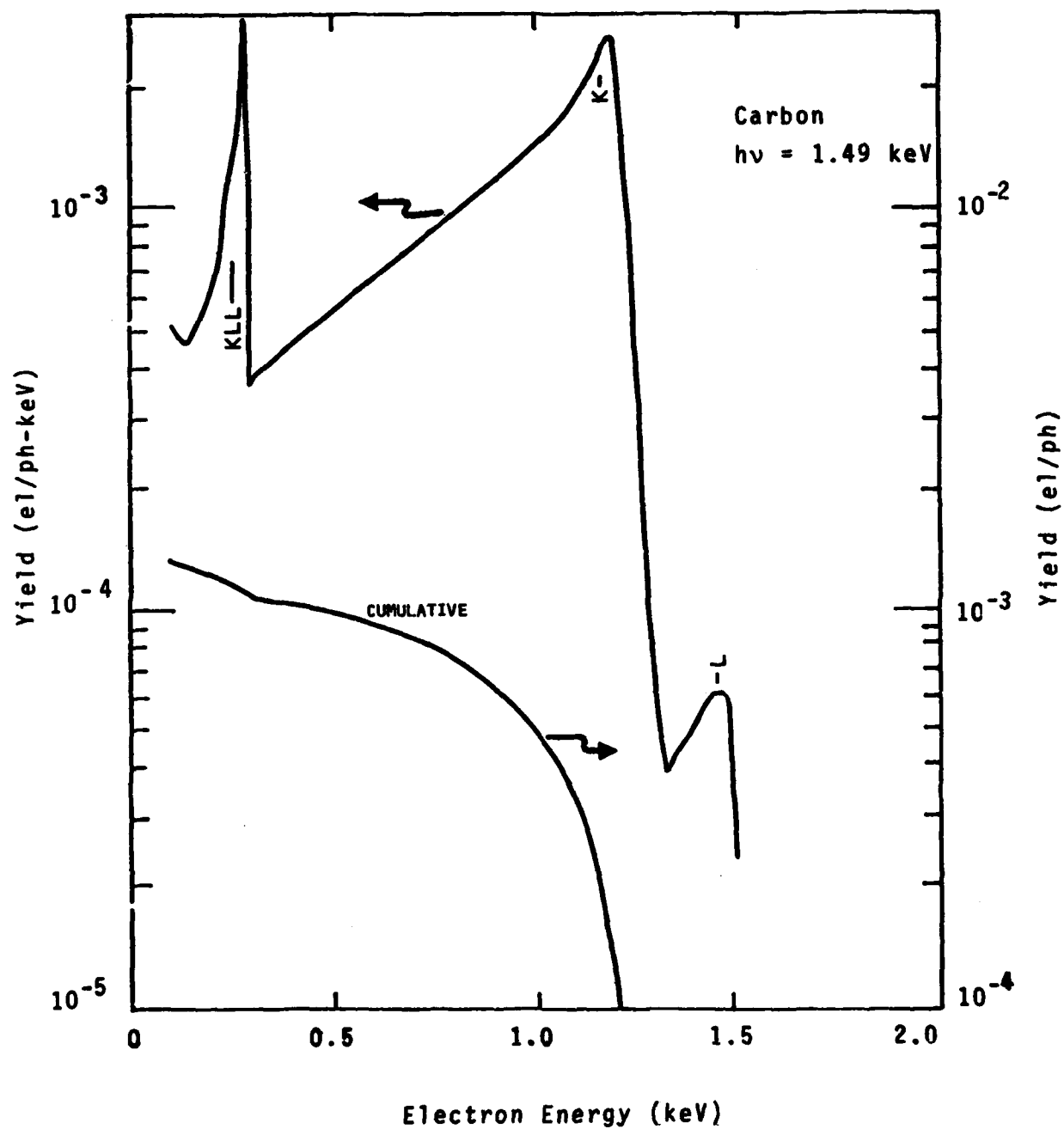


Figure 13 Photoemission spectrum and its cumulative yield for a 1.49 keV Gaussian photon source incident on C.



complex spectra are produced from the oxides due to the added features from oxygen. Overall, the presence of oxygen reduces the strength of photoemission since oxygen does not tend to photoionize in and above the soft X-ray region as readily as higher Z materials such as Al.

Figures 11 and 12 show spectra for the Sc K-line incident on Au and Ag. Again, such results allow for a demonstration of material effect, this time for much high Z materials ( $Z_{\text{Au}} = 79$ ;  $Z_{\text{Ag}} = 47$ ). Finally, Figure 13 provides an example of photoemission from C. The chosen source is the Al K-line at 1.49 keV. Unlike the higher Z materials, which can produce significantly different emission spectra as  $h\nu$  varies over the soft X-ray region, C will only produce the three features shown with K-photoelectrons dominating the emission.

### Section 3

#### INCORPORATING A SELF-CONTAINED ENERGY GRID SELECTION SCHEME INTO CODE SXR

One of the more difficult tasks undertaken in our overall program will be discussed in this section. That task has been to develop a scheme which provides a satisfactory electron energy grid for transport calculations using code SXR. We can report that we have successfully developed such a scheme. As a result, considerable time has been and will be saved in preparing the input data for SXR runs. The scheme provides good energy grids for either narrow or broad photon and electron sources for all materials so far modeled.

The difficulties in developing the above scheme stem from the following conditions:

- limited number of available grid points (currently 40)
- complex structure of photoelectron source spectra, and
- requirement that changes in grid interval sizes be gradual.

Figures 14 and 15 show examples of the complexity one can encounter in the source spectrum. For the case considered in Figure 14, a 5.4 keV Gaussian X-ray source is incident on Au. Figure 15 shows the spectrum

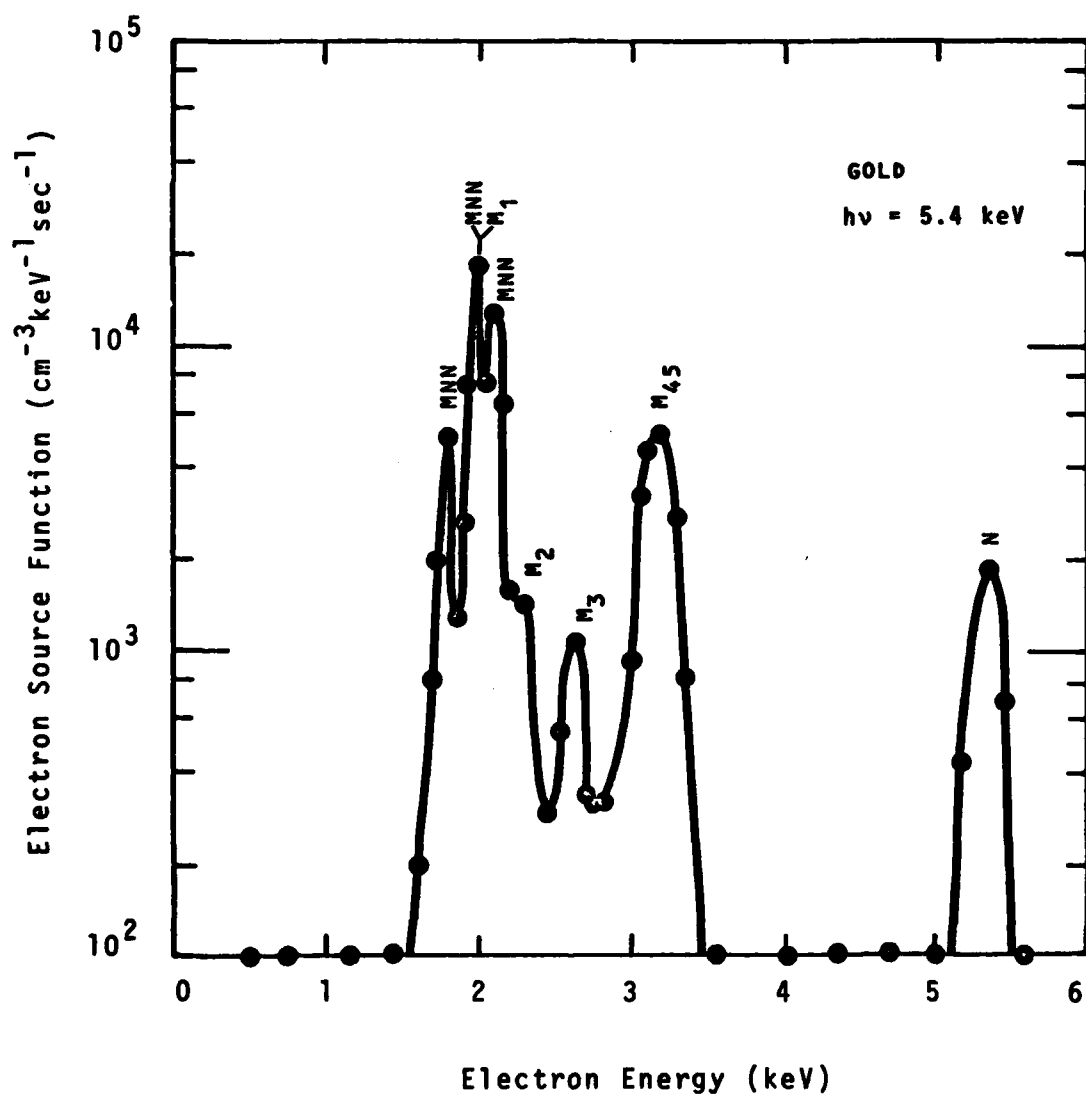


Figure 14 Electron source spectrum for a 5.4 keV Gaussian photon source incident on Au. Dots show grid determined by grid selection scheme.

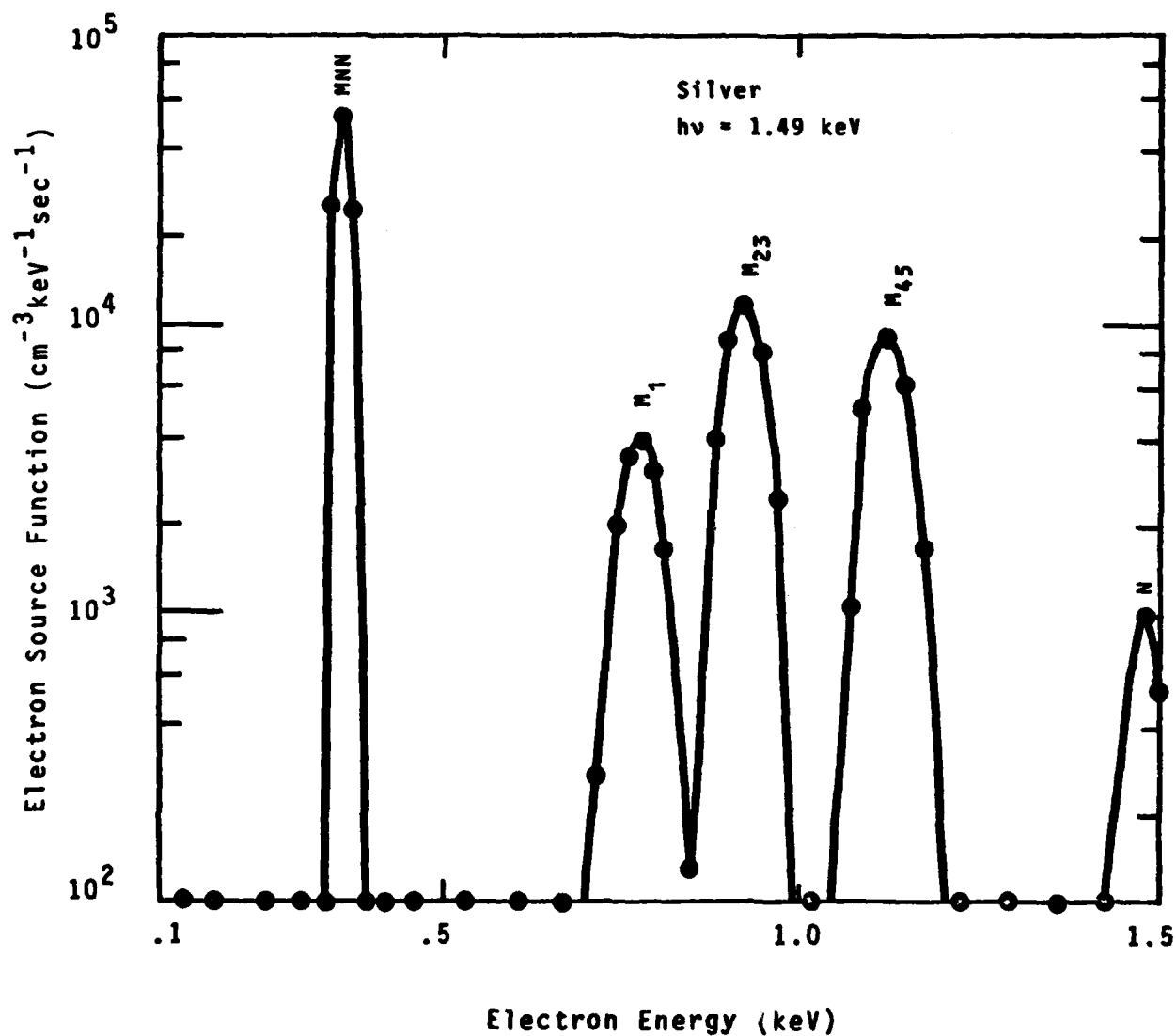


Figure 15 Electron source spectrum for a 1.49 keV Gaussian photon source incident on Ag. Dots show grid determined by grid selection scheme.

for a 1.49 keV Gaussian source incident on Ag. The grid points shown were selected by the code. The points on axis at the bottom of the figures are actually zeros. For completeness, the corresponding photoemission spectra are shown in Figures 16 and 17.

The third condition above is a requirement general to most transport formulations. Specific to that of SXR, it centers about the representations of the solution  $\phi(z, E, \mu)$  in the Boltzmann collision integral. To cast the integral into matrix form,  $\phi$  is given quadratic dependence versus  $\ln E$  and linear dependence versus direction cosine  $\mu$  over each  $E, \mu$  cell. With this quadratic dependence, one must be careful not to abruptly change the grid spacing in energy. Otherwise, unphysical structure may appear in the solution.

We will now proceed to describe the grid selection scheme in two stages. A brief overview will first be given in this paragraph then to be followed by selected details. We say selected since an attempt will not be made to provide a detailed documentation. Such an effort would be difficult due to the degree of logic required in the scheme. The high level called for arises from internal decisions such as when to merge features due to close proximity and from fulfilling such conditions as gradual grid interval variation throughout the entire energy range. We begin by noting that the scheme works on a logarithmic scale in energy. This is due to the way the solution  $\phi$  is represented in the collision integral (as noted above) and the capability of code SXR to handle energy ranges spanning

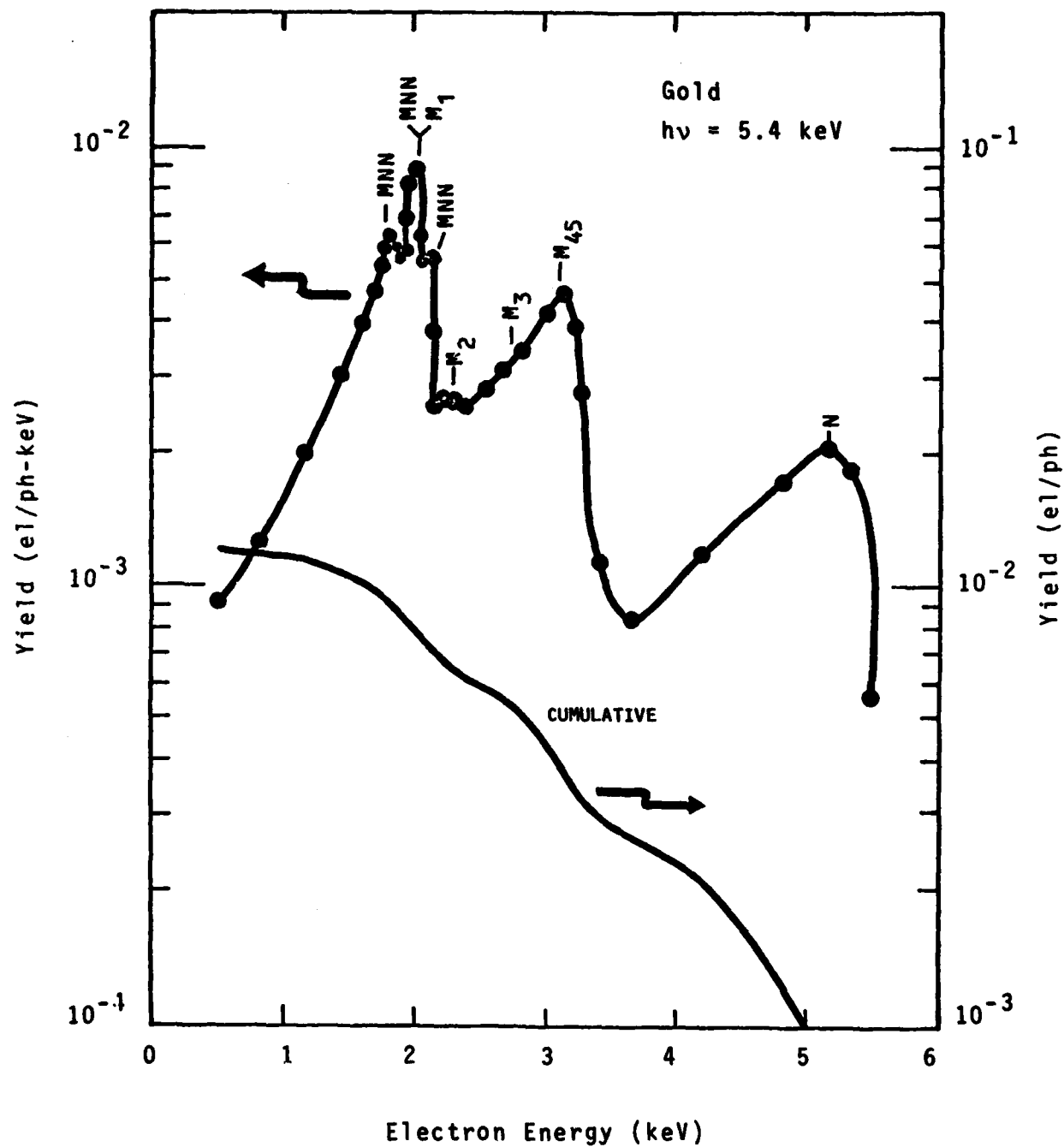


Figure 16 Photoelectron spectrum and its cumulative yield for a 5.4 keV Gaussian photon source incident on Au. Dots show grid determined by grid selection scheme.

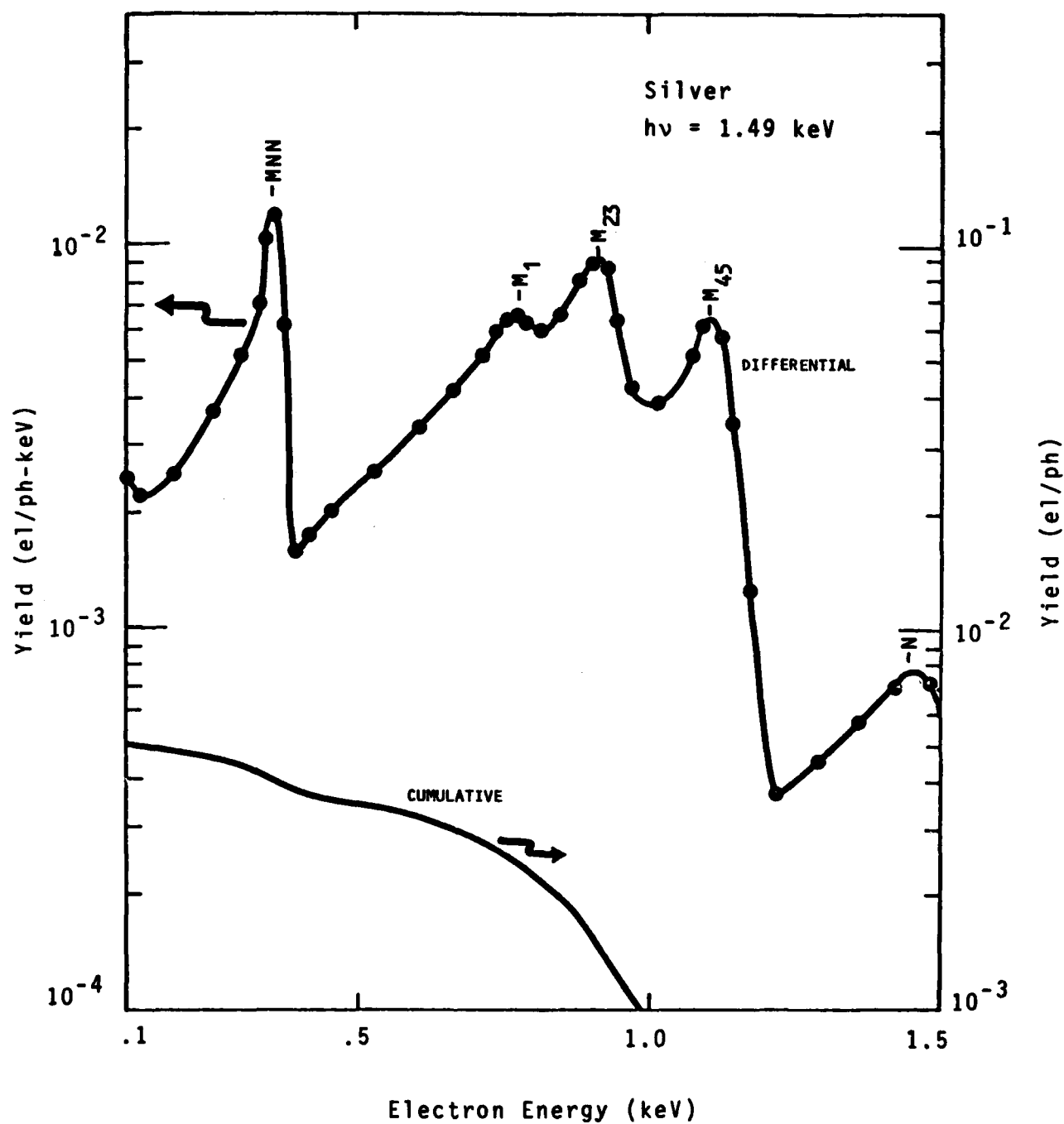


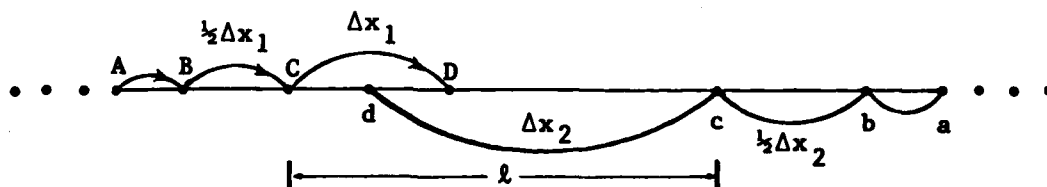
Figure 17 Photoelectron spectrum and its cumulative yield for a 1.49 keV Gaussian photon source incident on Ag. Dots show grid determined by grid selection scheme.

several decades. Grid selection on a logarithmic scale allows naturally for an increase in resolutions with decreasing energy. The grid selection begins with specification of what shall be referred to as principal points. These points give the energies at which the Auger and photoelectron features peak. The initial set of points is then examined in terms of strength and proximity of the various features. If the strength of a given feature is less than a given level relative to the other features, its principal point is removed. If two or more features are determined to be close together based on both the amount of overlap and their separation relative to the full energy range, all except one principal point are removed. A set of grid points is then specified for each principal point to characterize the given feature. Five such points, equally spaced, are used for Auger features. The number of points for photo features is variable but is no less than three. If a given photo feature is sharply peaked, more points are inserted within the structure. The final step is to add points between the adjacent principal point subsets in a way that achieves a smooth variation in adjacent grid spacings. We currently do not allow the ratio of adjacent intervals to lie outside the range .5 to 2. To achieve the required variations and keep the total number of grid points less than or equal to 40, an iteration technique is introduced which allows for adjustments in both the principal point subsets and the points between them.

The mathematical details of the essential logic for grid selection will be given in this



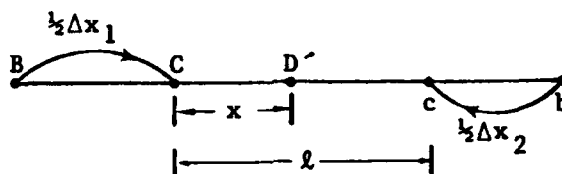
paragraph. Since the adjacent principal points are well-separated, we can assume that the interval between them is large enough that principal point subsets do not overlap. We want to add points starting from the sides of the interval. A comparison is first made between the sizes of the existing spacings on both sides. A point is added at the side adjacent to the smaller spacing in such a way that the size of the new spacing is twice as large as the previous one on this side. A comparison is again made between the size of this new spacing and the one on the other side, with a point then added to the side of the smaller spacing in the same fashion as before. This insertion procedure is stopped when the latest point from one side overshoots a point on the other side. For example, in the diagram below, point d from the right hand side



overshoots the point D inserted from the left hand side. The logic requires the removal of the two points D and d and determination of a new grid point at D' such that

$$X = CD' = \frac{\Delta x_1}{\Delta x_1 + \Delta x_2} l$$

as shown at the top of the next page.



The three spacings ratios  $CD':BC$ ,  $D'C:CD'$ , and  $cb:D'C$  are between .5 and 2. To prove this, we make use of the two given inequalities

$$\Delta x_1 < \Delta x_2 < 2\Delta x_1$$

and

$$2\Delta x_2 < l < \Delta x_1 + \Delta x_2$$

Then

$$\frac{CD'}{BC} = \frac{x}{\frac{1}{2}\Delta x_1} = \frac{2d}{\Delta x_1 + \Delta x_2} < 2$$

On the other hand

$$\frac{C'D'}{BC} = \frac{2d}{\Delta x_1 + \Delta x_2} > \frac{4\Delta x_1}{\Delta x_1 + \Delta x_2} = \frac{4}{1 + \frac{\Delta x_2}{\Delta x_1}} > \frac{4}{3}$$

For the next ratio,

$$\frac{D'C}{CD'} = \frac{d-x}{x} = \frac{\Delta x_2}{\Delta x_1}$$

which is between 1 and 2. The last ratio  $cb/D'c$  is, due to the way  $x$  is defined, equal to the first ratio  $CD'/BC$ .

## Section 4

### ADDITIONAL STUDIES DOCUMENTED IN PUBLICATIONS

The purpose of this section is to introduce and summarize the three papers represented in Appendices A-C. The first paper by Strickland and Lin<sup>8</sup> demonstrates the capability of code SXRPA to treat external soft electron sources. The two topics addressed are primary backscatter from Al and Au and charge and energy deposition in Teflon. The motivation for the backscatter analysis comes from our desire to critically test our scattering model for materials of high and low atomic number. The incident energy range considered is from .5 to 10 keV and good agreement is achieved in comparison with data. One comparison in the backscattered spectrum is made with code POEM<sup>17</sup> and there, good agreement is also obtained. The motivation for the calculations of deposition in Teflon comes from a charging analysis by Beers et al.<sup>18</sup>. A simple material model for Teflon is first developed but is not reported on in the paper. This will await further refinement which we hope to do as part of a future investigation of electron transport in polymers. Charge and energy deposition profiles are generated with code SXRPA for 2.5 and 5.0 keV electrons incident on Teflon and compared with the POEM results used by Beers et al. The main interest is in differences in penetration characteristics since these have a bearing on charge buildup. As expected, the SXRPA profiles extend further into the material due to

the code's treatment of straggling but the exhibited differences are not large.

The second paper by Lin and Strickland<sup>9</sup> discusses photoemission from Ag and C for the OWL II' source. Spectral and primary yield comparisons are made with the measurements by Bernstein<sup>11</sup>. These comparisons were previously reported in a recent DNA final report<sup>7</sup>. The extended analysis of Ag is reported for the first time in the paper. It came about from the factor of two difference in primary yield between the calculation and measurement. Following the analysis, we better understand transport properties in Ag and have more confidence in the calculations. The difference noted above still remains to be determined.

The third paper by Lin and Strickland<sup>10</sup> reports our latest material model for Ag. The discussion here is more theoretical than in the report by Strickland and Lin which introduced the model<sup>7</sup>. The model parameters in the paper also extend into the very soft X-ray region.

## REFERENCES

1. D. J. Strickland, "Soft X-Ray Photoemission," RADC-TR-77-252 (July 1977).
2. D. J. Strickland, IEEE Trans. Nuc. Sci., NS-24, No. 6, 2499 (1977).
3. D. J. Strickland and D. L. Lin, IEEE Trans. Nuc. Sci., NS-25, No. 6, 1571 (1978).
4. D. L. Lin, B. L. Beers and D. J. Strickland, IEEE Trans. Nuc. Sci., NS-25, No. 6, 1561 (1978).
5. D. J. Strickland, D. L. Lin, V. W. Pine and W. L. Chadsey, "Soft X-Ray Photoemission and Charge Deposition Near Material Interface," RADC-TR-78-183 (August 1978).
6. D. J. Strickland, D. L. Lin, T. M. Delmer, J. Rodgers, B. Goplen and W. L. Chadsey, "Soft X-Ray Photoemission, II," DNA Final Report (October 1977).
7. D. J. Strickland and D. L. Lin, "Soft X-Ray Photoemission Properties for the Newly Modeled Materials Gold, Silver, Copper and Carbon," DNA Final Report No. 4872 F (January 1979).
8. D. J. Strickland and D. L. Lin, IEEE Trans. Nuc. Sci., NS-26, No. 6, 4879 (1979).
9. D. L. Lin and D. J. Strickland, IEEE Trans. Nuc. Sci., NS-26, No. 6, 4984 (1979).
10. D. L. Lin and D. J. Strickland, J. Appl. Phys., to appear in March 1980 issue.
11. M. J. Bernstein, IEEE Trans. Nuc. Sci., NS-24, 2512 (1977).
12. M. J. Bernstein and J. A. Smith, IEEE Trans. Nuc. Sci., NS-25, No. 6, 1577 (1978).

#### REFERENCES (CONCLUDED)

13. M. J. Bernstein and J. A. Smith, IEEE Trans. Nuc. Sci., NS-26, No. 6, 4978 (1979).
14. E. P. Denisov, V. N. Shchemelev, A. N. Mezhevich and M. A. Rumsh, Fiz. Tver. Tela, 6, 2569 (1964) [Sov. Phys.-Solid State 6, 2047 (1965)].
15. R. R. Schaefer, J. Appl. Phys. 44, 152 (1973).
16. E. A. Burke, IEEE Trans. Nuc. Sci., NS-24, No. 6, 2505 (1977).
17. W. L. Chadsey, "POEM: A Fast Monte Carlo Code for the Calculation of X-ray Photoemission and Transition Zone Dose and Current," AFCRL-TR-75-0324 (15 January 1975).
18. B. L. Beers, H. C. Hwang, D. L. Lin and V. W. Pine, in "Proceedings of the USAF/NASA Spacecraft Charging Technology Conference," (1978).

## APPENDIX A



# ELECTRON TRANSPORT PROPERTIES FOR SOFT ELECTRON SOURCES INCIDENT ON CONDUCTING AND INSULATING MATERIALS\*

D. J. Strickland and D. L. Lin

RADIATION AND ELECTROMAGNETICS DIVISION  
SCIENCE APPLICATIONS, INC.  
Vienna, Virginia 22180

## INTRODUCTION

In this paper, we will address the basic problem of low energy electron transport in materials. By low energy, we are here referring to the low to subkeV energy region.

As a source, we consider electrons incident with distributions sufficiently narrow in energy to adequately simulate a mono-energetic condition. For the external electron source, three basic transport quantities of general interest are

- the primary backscatter yield (energy differential and energy integrated)
- primary current profile, and
- dose or energy deposition profile.

For selected materials we will be addressing each of these quantities. To do so, we apply the transport code SXRP which provides for a rigorous description of transport down to sub-keV energies. From SXRP will come backscatter results for Al and Au and current and dose profile information for Teflon (CF<sub>2</sub>).

The code SXRP and its applications are by now fairly well documented.<sup>1-7</sup> Its primary application to date has been to the problem of soft X-ray photoemission. The transport description is provided by the Boltzmann equation which is solved for the electron flux  $\phi(z, E, \mu)$  in e/cm<sup>2</sup>-s-eV-sv. The arguments of  $\phi$  are depth (z), energy (E) and direction cosine ( $\mu$ ). The given formulation allows for the production of photo-, Auger and Compton electrons by photons and for the following effects involving electrons:

- scattering through any angle,
- discrete energy loss, and
- production of Auger and secondary electrons.

SXRP is thus capable of investigating transport effects down to energies well below the cutoff imposed by the continuous slowing down approximation (CSDA) which is commonly used in other formulations.

There are two prime motivating factors for the work to be discussed in this paper:

- (1) electron backscatter is sensitive to the scattering and energy loss characteristics of a given material and consequently provides a good test on the material model needed to perform the transport, and
- (2) the previous work by Beers, et al.<sup>8</sup> on electron charging in Teflon.

The backscatter analysis is thus basically a material model validation exercise. Al and Au have been chosen for this analysis since most of our efforts to date have concentrated on these materials. Beyond validating our models, the analysis also improves our basic understanding of transport properties down to sub-keV energies and demonstrates the applicability of code SXRP to external electron as well as X-ray sources.

The work by Beers, et al. addressed the general problem of spacecraft charging. One part of their analysis dealt with the equilibrium charge distribution in Teflon for a 2.5 keV electron source. The needed current and dose profiles were obtained using the Monte Carlo transport code POEM.<sup>9</sup> Since the code SXRP is well suited to treating a source as low in energy as the above, a simple Teflon model was developed and applied to the same problem. We were primarily interested in seeing how different the penetration characteristics would be between the two approaches. This work will report our first such results and show a comparison with the POEM results.

## MATERIAL MODEL PARAMETERS

The following parameters are needed in our formulation to describe electron interactions:

- elastic scattering differential inverse mean free path (DIMFP),
- plasmon DIMFP,
- conduction/valence band DIMFP, and
- inner shell DIMFP's.

A discussion will follow which describes how we currently specify the elastic DIMFP. We have previously described how the other parameters are specified and thus their description here will be brief. Basically, the plasmon and conduction/valence band DIMFP's are obtained from the dielectric response function as modeled by Ritchie and his colleagues.<sup>10,11</sup> The inner shell DIMFP's (DIMFP's integrated over either energy loss or secondary electron energy) are obtained from their corresponding photoionization cross sections by the method described by Lin, et al.<sup>4</sup> The differential dependence in energy loss is that given by Strickland, et al.<sup>12</sup> The results for Al and Au from applying these techniques have already been presented elsewhere.<sup>2,4,7</sup> The Teflon DIMFP's, however, are new but relatively untested and we thus defer to a later date their presentation.

We use the screened Rutherford formula to specify the elastic scattering DIMFP. Its form is given by

$$K_{\text{elas}}(E, \theta) = K_{\text{elas}}(E) p(E, \theta) \text{ cm}^{-1} \text{sr}^{-1} \quad (1)$$

\*This work was supported by the DEFENSE NUCLEAR AGENCY under Contract Number DNA001-77-C-0209

where

$$p(E, \theta) = \frac{\eta(\eta+1)}{\pi} \frac{1}{(1-\cos\theta+2\eta)^2} \quad (2)$$

$p(E, \theta)$  is the normalized Rutherford formula and  $\eta$  is the screening parameter which contains the energy dependence in  $p$ .  $K_{elas}(E)$  has the form

$$K_{elas}(E) = n \frac{Z^2 e^4}{v^2 p} \frac{\pi}{\eta(\eta+1)} \quad (3)$$

where  $v$  and  $p$  are respectively the electron velocity and momentum corresponding to  $E$ ,  $Z$  is the atomic number, and  $n$  is the material number density. The screening parameter  $\eta$  may be represented in the form

$$\eta(e) = 4.3 Z^{2/3} \frac{\eta_c}{E} \quad (4)$$

where  $E$  is in eV and  $\eta_c$  is a function of the screening potential. The screening potential in conducting solids can be adequately represented by a single Yukawa potential which leads to constant  $\eta_c$ .<sup>13</sup> We have previously used  $\eta_c = 1$  since values close to unity have been applied before.<sup>14,15</sup> We now use the value 3.2, however, since it is based directly on considerations of the screening potential itself.<sup>13</sup>

The elastic IMFP from Eq. 3 and the screening parameter  $\eta$  are shown in Fig. 1 for both Al and Au over the range of 0.1 to 10 keV. The point of showing these results is to emphasize the contrast between Al and Au in their scattering characteristics. Both the elastic collision frequency and mean angle of scattering per collision are larger for Au. We have not bothered showing  $K_{elas}$  and  $\eta$  for Teflon since their variations with energy will look similar to those in Fig. 1. The needed results are obtained with the above equations for  $Z$  values of 6(C) and 9(F) and for the appropriate number densities of these elements.

A word of caution is appropriate here regarding these results at low energies. Eq. (3) with  $\eta$  given by Eq. (4) may become increasingly inaccurate with decreasing energy since these expressions apply to the Born region which, though  $Z$  dependent, is generally above the low keV region. For lack of definitive and comprehensive information on  $K_{elas}$  at low energy, we choose to stay with expressions (2)-(4) which not only are particularly convenient to work with, but also express the isotropic nature of acoustic phonon scattering generally accepted for electron energies of a few eV.

#### ENERGY AND ANGULAR DEPENDENCE OF THE INCIDENT ELECTRON FLUX

We wish to consider incident electron fluxes narrow in both energy and angle since in the experimental situation, nearly monoenergetic and normal incidence conditions usually exist. SXRP, however, can only approximate these conditions, the extent of which depends on the number of grid points chosen in the above variables. The code is currently set up to handle a maximum of 40 energy and 20 angular points. For past photoemission work, these numbers have been more than adequate for satisfactory comparison of results with measurements. The same still holds true for backscatter results in terms of the energy variable since backscatter characteristics are slowly varying in energy. This is not the case, however, in the angular variable due to the sensitivity of the backscatter yield with the angle of incidence. Rather than increase the

maximum number of angles which SXRP can handle, we choose, for the sake of saving computing time, instead to apply corrections to our backscatter results for comparisons with measurements. The corrections are based on available data and will be further discussed below.

As distributions finite in width, we have chosen normalized Gaussian distributions for characterizing the incident electron flux. Designated by  $\phi_0$ , the incident flux is given by

$$\phi_0(E, \mu) = f(E)g(\mu) \quad \text{el/cm}^2\text{-s-eV-sr} \quad (5)$$

where

$$f(E) = \frac{1}{\pi\alpha} e^{-\frac{(E-E_0)^2}{\alpha}} \quad (6)$$

and

$$g(\mu) = \frac{2}{\beta(\pi-\beta)} e^{-\frac{(1-\mu)^2}{\beta}} \quad (7)$$

These functions are normalized to give a total incident flux of 1 el/cm<sup>2</sup>-s. The parameters  $\alpha$  and  $\beta$  control the widths of the distributions while the parameter  $E_0$  gives the energy at which  $\phi_0$  peaks. We have considered a number of sets of  $E_0$  and  $\alpha$  which are shown in Table 1. The absolute width of  $f(E)$  is allowed to broaden as  $E_0$  increases which leads to the variation in  $\alpha$  as shown.

We consider only one  $\beta$  value in this work, namely,  $\beta=0.2$ . We feel that this is about as small as the value should be, given a maximum of ten angles per hemisphere. To adjust our yields to normal incidence, we fold the following expression into the above  $g(\mu)$ :

$$Y(\mu) = B \frac{Y(1)^\mu}{B} \quad (8)$$

This expression comes from Darlington<sup>16</sup> who assigned  $B$  the value 0.891. Darlington arrived at Expression (8) and the above value of  $B$  by considering data for incident energies above 9.3 keV. We expect them to remain adequate down to at least 1 keV since yield data, in general, do not show much variation from the 10 keV range on down to this energy. Departures that may take place should be in the direction of weaker  $\mu$  dependence since the mean scattering angle increases with decreasing energy.

#### BACKSCATTER FROM AL AND AU

The information to be presented in this section, although not contributing significant new insights into emission characteristics of materials for external electron sources, is important for assessing the overall validity of our formulation, material models, and the SXRP code itself. A comparison of backscatter results with measurements provides one of the most critical tests that can be made on the scattering model in a given formulation.

The significance of such a test lies in the fact that scattering is one of the most important processes in electron transport be it either to problems dealing with photon or electron sources. One cannot begin to reasonably predict current and dose characteristics within materials for electron sources without taking it into consideration. The situation is less critical for photon sources but scattering still does have a

pronounced effect on such quantities as primary yield and its associated spectral behavior.<sup>5</sup>

Here, we will concentrate on primary yield results for Al and Au between 0.5 and 20 keV. This range is and has been of particular interest to us in characterizing photoemission properties of materials such as the above as well as  $\text{Al}_2\text{O}_3$ ,  $\text{SiO}_2$ , Ag, Cu and C. For code validation purposes, Al and Au are particularly desirable since they provide cases of low Z ( $Z_{\text{Al}} = 13$ ) and high Z ( $Z_{\text{Au}} = 79$ ) and are materials for which extensive measurements have been made.

Fig. 2 presents our calculated primary backscatter yield curves for Al and Au from 0.5 to 20 keV. They appear together with the measurements taken from Fitting<sup>17</sup> and with predictions from the code POEM. Other measurements have also been reported in the literature but are not included here since most of them closely follow Fitting's results (see Burke<sup>18</sup> for a recent tabulation of the data). The calculated values include contributions down to 0.1 keV and have been adjusted to normal incidence using Eq. (8) with  $Y(1)$  in that equation taken from the data in Fig. 2. POEM yield results for Au are not shown below 10 keV and for Al not below 2 keV since they begin to rapidly decrease below these energies. The lower limit of applicability of this code is seen to have a pronounced Z dependence. This indicated trend would suggest, however, that POEM should give an adequate transport description down to a few keV for the third material addressed in this paper, namely, Teflon. We will show that this is, in fact, the case in the next section. Returning to Fig. 2, the overall agreement between the SXRP yields and the data is good although trends with energy are somewhat different. If one accepts the data trends, the comparisons suggest we overestimate scattering for Au and underestimate it for Al at low energies relative to the loss processes. If this is, in fact, the case, we do not know at this time whether our scattering description or our energy loss description is the more responsible for the given differences.

Figure 3 gives examples of differential yields or backscattered spectra for 5 keV electrons incident on the two materials. Cumulative yields are shown below the spectra and give the unadjusted primary yield values on the left. The Au spectrum is seen to be less energy degraded due to the stronger scattering properties of this material.

Figure 4 offers a comparison between SXRP and POEM spectra for the same 5 keV source incident on Al. Both sets of results apply to the non-normal incidence case described by  $g(u)$  in Eq. (7). Good agreement in spectra and yields is obtained in spite of the diverse methods applied and strongly energy degraded nature of the spectra.

#### CURRENT AND DOSE PROFILES IN TEFLON

In this section, we consider 2.5 and 5 keV electrons incident on Teflon which we have simply modeled as a mixture of C and F in their appropriate amounts. Calculated current and dose profiles will be presented and compared with similar results obtained with the POEM code. Our initial interest in using SXRP to address this problem was to see how much effect straggling would have on these profiles. POEM does not treat this effect and, consequently, its calculated current and dose become identically zero at a depth of one electron range into the material. SXRP is ideally suited to investigate depth effects since it rigorously allows for straggling through its discrete energy loss description and because of its method of solving the Boltzmann transport equation. The method is based on a

eigenvalue approach which can be expected to be superior to either finite difference or Monte Carlo schemes for specifying transport characteristics deep in the material.

The results to follow are based on two simple constraints we have forced upon our initial material model for Teflon. These are:

- the inelastic DIMFP's give the Bethe stopping power above several keV, and
- the elastic DIMFP, for the given inelastic DIMFP's, give a good primary backscatter yield (~15% in low keV region).

These are important constraints since by experience, we have found that penetration characteristics are quite sensitive to the ratio of, say, the elastic IMFP to the stopping power.

Figure 5 shows SXRP and POEM current and dose profiles for 2.5 keV electrons incident on Teflon. Figure 6 shows similar results for 5 keV electrons. In general, good agreement is obtained between the two different transport models. The SXRP results are seen to extend deeper into the material, as expected, due to the effect of straggling. A pronounced difference is not produced, however, by this effect. The largest differences occur in dose near the front face. Some enhancement in the SXRP dose will occur due to its source not being purely normally incident. This will not, however, explain the bulk of the difference. We believe it is due to energy deposition below ~1 keV which is included in SXRP's description, but not in POEM's due to the high energy nature of that code.

To summarize this section, overall good agreement between SXRP and POEM has been obtained in current and dose profiles in Teflon. We wish to stress, however, that our material model for Teflon has just been developed, is simple in nature, and as of now is not well validated. Furthermore, we have found that the current and dose profile behaviors are quite sensitive to changes in the scattering and energy loss descriptions within this model. Thus, as our model becomes more refined and, in turn, better validated, some changes may occur in our results.

#### SUMMARY AND CONCLUSIONS

In this paper, we have reported on two recent analyses carried out using the code SXRP to treat external electron sources. The first analysis concerned backscatter from Al and Au and was undertaken to critically test the scattering and energy loss characteristics in our material models. We feel the test was successful based on the agreement obtained with published primary backscatter yield data between 0.5 and 20 keV. Since photoemission characteristics are less sensitive to transport parameters than those for backscatter, these tested models, as used by code SXRP, should be especially valid for the problem of photoemission. This has already been indicated by the agreement obtained with the available published photoemission data.

The second analysis concerned current and dose profiles in Teflon and was undertaken to test one aspect of a charging calculation by Beers, et al.<sup>8</sup> concerned with the larger problem of spacecraft charging. The points of this analysis were to determine the applicability of code SXRP to specifying internal transport characteristics, but more specifically to see how important straggling is to the above profiles since their fall-off behavior deep in the material is important to the

applied charging model. Beers, et al. had used the transport code POEM to obtain their current and dose profiles which does not permit an electron to go beyond one CSDA range. We found that the SKRP calculated profiles do extend deeper into the material due to straggling, but that, in general, the agreement with the POEM results was good except near the front surface. This conclusion is somewhat conditional based on our present material model for Teflon which has just been developed and is in need of further work.

#### REFERENCES

1. D. J. Strickland, "Soft X-Ray Photoemission," RADC-TR-77-252 (July 1977).
2. D. J. Strickland, *IEEE Trans. Nuc. Sci.*, **NS-24**, No. 6, 2499 (1977).
3. D. J. Strickland and D. L. Lin, *IEEE Trans. Nuc. Sci.*, **NS-25**, No. 6, 1571 (1978).
4. D. L. Lin, B. L. Beers and D. J. Strickland, *IEEE Trans. Nuc. Sci.*, **NS-25**, No. 6, 1561 (1978).
5. D. J. Strickland, D. L. Lin, V. W. Pine and W. L. Chadsey, "Soft X-Ray Photoemission and Charge Deposition Near Material Interface," RADC-TR-78-183 (August 1978).
6. D. J. Strickland, D. L. Lin, T. M. Delmer, J. Rodgers, B. Coplen and W. L. Chadsey, "Soft X-Ray Photoemission, II," DMA Final Report (October 1977).
7. D. J. Strickland and D. L. Lin, "Soft X-Ray Photoemission Properties for the Newly Modeled Materials Gold, Silver, Copper and Carbon," DMA Final Report (January 1979).
8. B. L. Beers, H. C. Hwang, D. L. Lin and V. W. Pine, in "Proceedings of the USAF/NASA Spacecraft Charging Technology Conference," (1978).
9. W. L. Chadsey, "POEM: A Fast Monte Carlo Code for the Calculation of X-ray Photoemission and Transition Zone Dose and Current," AFRL-TR-75-0224 (15 January 1975).
10. C. J. Tung and R. H. Ritchie, *Phys. Rev. B* **16**, 4302 (1977).
11. C. J. Tung, C. J. Ashley, R. D. Birkhoff, R. H. Ritchie, L. C. Emerson and V. E. Anderson, *Phys. Rev. B* **16**, 3049 (1977).
12. D. J. Strickland, D. L. Book, T. P. Coffey and J. A. Fedder, *J. Geophys. Res.*, **81**, 2755 (1976).
13. B. P. Nigam, M. K. Sundaresan and Te-You Wu, "Theory of Multiple Scattering: Second Born Approximation and Corrections to Moliere's Work," *Phys. Rev.* **115**, 491 (1959).
14. M. J. Berger, S. M. Seltzer and K. Maeda, "Energy Deposition by Auroral Electrons in the Atmosphere," *J. Atmos. Terr. Phys.*, **32**, 1015 (1970).
15. H. E. Bishop, "Electron Scattering in Thick Targets," *Brit. J. Appl. Phys.*, **18**, 703 (1967).
16. E. H. Darlington, *J. Phys. D. Appl. Phys.*, **8**, 85 (1975).
17. H. J. Fitting, *Phys. Stat. Sol. (a)*, **26**, 525 (1974).

18. E. A. Burke, *IEEE Trans. Nuc. Sci.*, **NS-24**, No. 6, 2505 (1977).

TABLE 1. ENERGY PARAMETERS FOR INCIDENT ELECTRON FLUXES

$E_0$ (keV)	$\alpha$ (keV)	MATERIALS
0.5	0.025	AL, AU
1.0	0.05	AL, AU
2.0	0.10	AL, AU
2.5	0.11	TEFLON
5.0	0.25	AL, AU, TEFLON
10.0	0.50	AL, AU
20.0	1.00	AL, AU

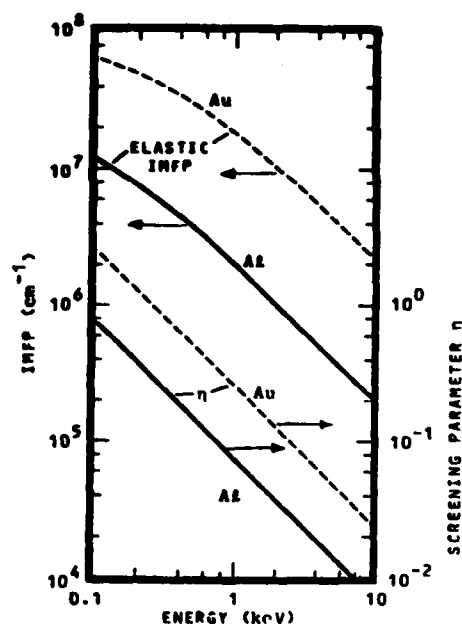


FIGURE 1. ELASTIC INVERSE MEAN FREE PATHS AND SCREENING PARAMETER  $\eta$  FOR AL AND AU

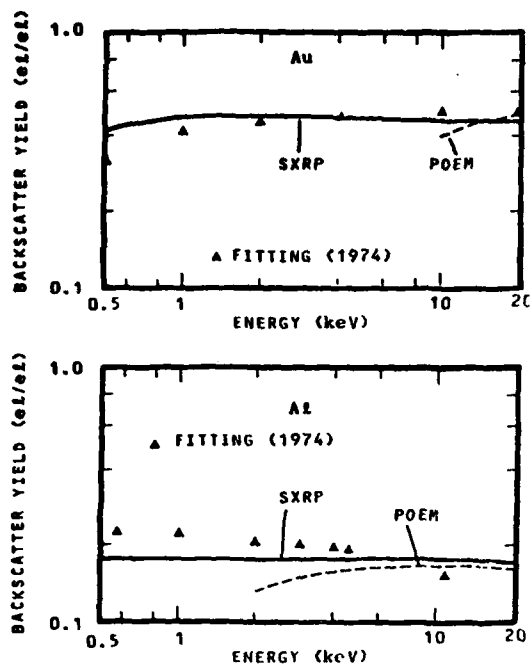


FIGURE 2. ELECTRON BACKSCATTER YIELDS FOR AL AND Au FROM 0.5 TO 20 keV

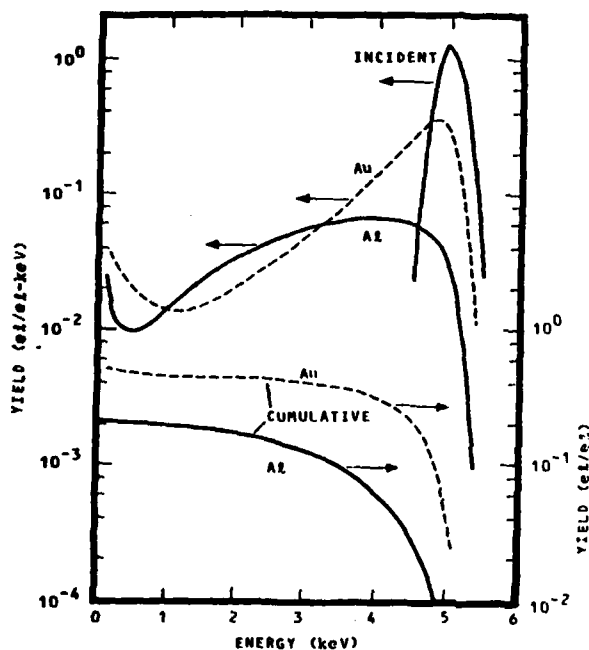


FIGURE 3. DIFFERENTIAL AND CUMULATIVE BACKSCATTER YIELDS AS CALCULATED BY CODE SXRP FOR A 5 keV GAUSSIAN ELECTRON SOURCE INCIDENT ON AL AND Au

These results have not been adjusted to normal incidence from the Gaussian type of incident angular dependence.

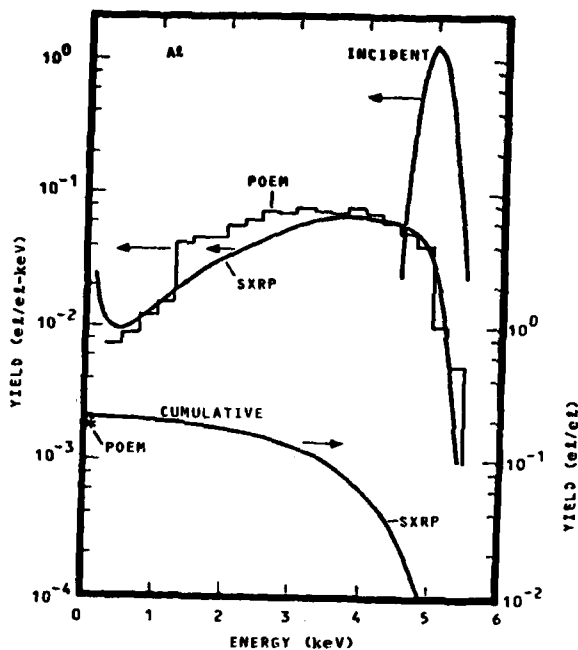


FIGURE 4. DIFFERENTIAL YIELDS AS CALCULATED BY THE CODES SXRP AND POEM FOR A 5 keV GAUSSIAN ELECTRON SOURCE INCIDENT ON AL

Also shown are SXRP's cumulative yield and POEM's primary yield. These results (including POEM's), like those in Figure 3, have not been adjusted to normal incidence.

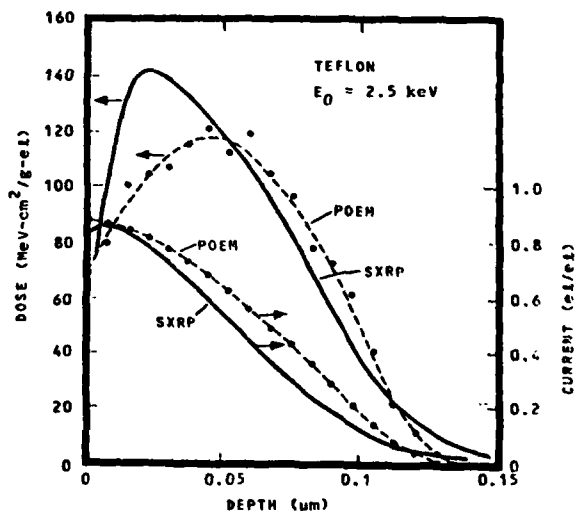


FIGURE 5. CURRENT AND DOSE PROFILES AS CALCULATED BY THE CODES SXRP AND POEM FOR 2.5 keV ELECTRONS INCIDENT ON TEFLON

The dots give the POEM results while the dashed curves give fits to these results.

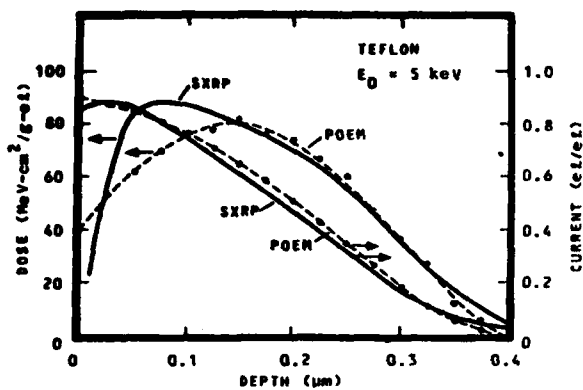


FIGURE 6. SIMILAR TO FIGURE 5 EXCEPT FOR 5 keV ELECTRONS INCIDENT ON TEFLON

## APPENDIX B

PHOTOEMISSION FROM Ag AND C FOR AN  
EXPLODING WIRE RADIATOR SOURCE\*D. L. Lin and D. J. Strickland  
RADIATION AND ELECTROMAGNETICS DIVISION  
SCIENCE APPLICATIONS, INC.  
Vienna, Virginia 22180

## INTRODUCTION

In this paper, we will discuss the problem of soft X-ray photoemission for the materials Ag and C. In particular, we will be presenting calculated photoemission spectra and total primary photoemission yields for an exploding wire radiator (EWR) source. The EWR source of interest is generated by the OWL II' flash X-ray facility and has been used over the last couple of years by the DEFENSE NUCLEAR AGENCY to investigate SCEMP response in the soft X-ray region.

The photoemission calculations have been carried out using the code SXRP which provides for a rigorous description of electron transport to energies well below a kilovolt. For a description of the code, we refer the reader to the various publications and reports which document the formulation and the various applications.<sup>1-8</sup> For the EWR source, we are able to compare our spectra with the spectrometer data of Bernstein<sup>9</sup> and our total primary yields both with the data of Bernstein and Fromme, et al.<sup>10</sup>

Last year, we reported on EWR photoemission results for the materials Al and Au.<sup>3</sup> At that time, it was not possible to include analyses for Ag and C since the needed SXRP material models had not yet been developed. Since this is the first paper addressing SXRP results for these newly modeled materials, we choose here to also present model information. A fairly good description of what a given model contains may be found in last year's paper.<sup>3</sup>

## MATERIAL MODELS FOR Ag AND C

Given an incident photon spectrum, the ejected electrons consist of two types — photoelectrons and Auger electrons. Photoelectrons from different subshells have associated with them different photoionization cross sections and binding energies. Subshell photoionization cross sections are therefore needed. Unfortunately, compilations of theoretical and experimental results are all in the form of the total photoionization cross section.<sup>11-13</sup> Selected calculations, however, for individual subshells do exist.<sup>14-18</sup> Complete compilation of the photoionization cross sections for all elements, all subshells, and all desirable energies are prohibitive. We have recently developed and modified a code to calculate the desired cross sections using Herman Skillman potentials and wave functions. The performance of this code is satisfactory in the sense that the sum of the subshell cross sections does agree with experiments for photon energies in the low to sub-keV range.

Auger energies and yields are obtained from spectroscopy experiments<sup>17</sup> and a compilation.<sup>11</sup> We have listed in Tables 1 and 2 the binding energies and Auger features for the respective materials, Ag and C.

\*This work was supported by the DEFENSE NUCLEAR AGENCY under Contract Number DNA001-77-C-0209.

For inner shell inverse mean free paths (IMFP), we have employed a technique<sup>4</sup> which provides a relationship between the impact IMFP and the corresponding subshell photoionization cross section. In the case of conductors, e.g., Ag, the IMFP's for conduction band ionization and plasmon excitation are obtained from the dielectric response function as modeled by Ritchie and his colleagues.<sup>18,19</sup> The IMFP's for Ag are shown in Figure 1. The IMFP's for conduction band ionization and plasmon excitation are obtained by assigning the single 0 shell electron to the conduction band. It is important that our total IMFP curve agree with existing data, also shown on the same figure.

For carbon, the electron impact IMFP's for inner shells, as calculated by the above cited method, are shown in Figure 2. An insulator model has been developed by Ashley, et al.<sup>19</sup> for the IMFP's of polystyrene and its results are also shown in Figure 2. The agreement is satisfactory considering the diversity in the approaches used.

The elastic IMFP is given by the screened Rutherford formula. Values for Ag and C may be seen in Figure 3 where they appear with the total inelastic IMFP's from Figures 1 and 2. Elastic scattering is seen to be more dominant in Ag due to its higher Z value. For more information on our treatment of elastic scattering, we refer the reader to the companion paper by Strickland and Lin<sup>8</sup> and to the report by Strickland, et al.<sup>5</sup>

## RESULTS

The X-ray source spectrum used in the calculation of the photoemission yields is the same one appearing in last year's paper on photoemission.<sup>3</sup> It is a continuum representation of an actual OWL II' X-ray spectrum with a prominent feature at ~1.65 keV containing ~50% of the energy. For this source representation, Figures 4 and 5 show the calculated photoemission spectra, those measured by Bernstein,<sup>9</sup> the calculated cumulative yields, and measured primary yields by Bernstein and Fromme, et al.<sup>10</sup> for C and Ag.

The dominant feature in the C spectrum comes from K photoelectrons arising from ionization by the X-rays in the strong 1.64 keV feature in our source representation. At low energies, a feature appears due to the production of KLL Auger electrons following photoionization of the K shell.

The dominant feature in the Ag spectrum comes from M photoelectrons and Auger electrons following photoionization of the M and L shells. The M peaks correspond to the 1.64 keV source feature while the region above, until the LPM peak is reached, corresponds to the continuum region of the source spectrum above 1.65 keV.



The agreement between us and Bernstein is good for C as can be seen in Figure 4. There is also reasonable agreement with Fromme's back-biased diode data. For Ag, the agreement in spectral shape between us and Bernstein is also good as can be seen in Figure 5. Our yield, however, is about half of both Bernstein's and Fromme's higher value. There are a number of potential sources for this difference, such as uncertainties in the X-ray source spectrum. We are not in a convenient position to assess those uncertainties associated with either the source or the photoemission experiments. We have, however, undertaken an assessment of the accuracy of our own results and this will appear next.

#### ACCURACY ASSESSMENT OF THE Ag RESULTS

Unlike the previously investigated materials Al and Au, we have not found published data for Ag on the primary photoemission yield at X-ray energies falling within the EWR energy region. We have thus chosen to make a consistency check between the Ag EWR results and those for Au. We have chosen Au because:

- we obtain good agreement with the published photoemission data, and
- transport properties are similar between Ag and Au, as will be demonstrated.

To examine consistency in photoemission from one material to the next, one must compare photoelectron source spectra and transport properties. Figure 6 provides for a comparison of such spectra for the assumed EWR source incident on Ag and Au. The Ag spectrum is seen to be both weaker and softer. Its integrated value is  $1.3 \times 10^4$  el/cm<sup>2</sup>-s (for unit incident flux) and its mean energy is 1.3 keV compared to values of  $4.7 \times 10^4$  el/cm<sup>2</sup>-s and 1.5 keV for Au. If transport properties were identical for these materials, the given electron source differences would lead to  $\sim 3.3$  times larger yield for Au compared to the actual calculated value of 3.6.

To examine differences in transport properties, photoemission spectra were obtained for both materials with the same electron source, namely, the Ag source in Figure 6. These results appear in Figure 7 and demonstrate that transport characteristics, for the type of source we are considering, are quite similar for Ag and Au. Thus, differences in the photoelectron production rates for these materials are primarily responsible for differences in yields. From the previous paragraph, we see that for the assumed material model parameters, we do have consistency in photoemission predictions between Ag and Au. Regarding model parameters, we believe our photoionization cross sections are accurate since their sum agrees with the published data. In turn, we expect that our calculated electron source spectrum is reasonably accurate.

Returning to the factor of two discrepancy between the calculated and measured yield for Ag, there are, of course, uncertainties in both the calculations and measurements, as well as in X-ray source definition. We do not know the cause of the difference at this time, but are confident, for the assumed X-ray source spectrum, that the calculated yield is accurate to better than a factor of two following the above described analysis.

#### SUMMARY AND CONCLUSIONS

In this paper, we have presented the material model parameters for C and Ag needed by code SXRP to investigate soft X-ray photoemission. Using these models, photoemission spectra and yields have been obtained for an EWR source and compared with the data of Bernstein and Fromme, et al. We obtain good agreement with the spectral data for both C and Ag, good agreement in yield for C, but find the yield data for Ag to be about twice the calculated value. A consistency test was then applied to our Ag results by introducing our previously calculated Au photoemission yield which agrees well with the data. We found, by comparing the Ag and Au electron source spectra and transport properties, that their yields are consistent with one another for the assumed material models. We thus conclude that for the assumed EWR X-ray spectrum, the calculated Ag yield should be accurate to better than the factor of two discrepancy exhibited.

An estimate of the contamination effect for Ag based on our results of Al and Al<sub>2</sub>O<sub>3</sub>, indicates that the photoemission yield of the contaminated Ag will be lower than reported here.

In summary, we have compared, to date, our photoemission results with the data for an EWR source incident on Al, Au, C, and Ag (Al and Au results previously presented<sup>3</sup>). In general, the agreement in spectral behavior between our calculations and Bernstein's measurements is good. With the exception of Ag, agreement is also satisfactory between our primary yield values and the available data.

#### REFERENCES

1. D. J. Strickland, "Soft X-ray Photoemission," RADC-TR-77-252 (July 1977).
2. D. J. Strickland, *IEEE Trans. Nuc. Sci.*, **NS-24**, No. 6, 2499 (1977).
3. D. J. Strickland and D. L. Lin, *IEEE Trans. Nuc. Sci.*, **NS-25**, No. 6, 1571 (1978).
4. D. L. Lin, B. L. Beers, and D. J. Strickland, *IEEE Trans. Nuc. Sci.*, **NS-25**, No. 6, 1561 (1978).
5. D. J. Strickland, D. L. Lin, V. W. Pine, and W. L. Chadsey, "Soft X-ray Photoemission and Charge Deposition Near Material Interfaces," RADC-TR-78-183 (August 1978).
6. D. J. Strickland, D. L. Lin, T. M. Delmer, J. Rodgers, B. Goplen, and W. L. Chadsey, "Soft X-ray Photoemission, II," DNA Final Report (October 1977).
7. D. J. Strickland and D. L. Lin, "Soft X-ray Photoemission Properties for the Newly Modeled Materials Gold, Silver, Copper, and Carbon," DNA Final Report (January 1979).
8. D. J. Strickland and D. L. Lin, "Electron Transport Properties for Soft Electron Sources Incident on Conducting and Insulating Materials," *IEEE Trans. Nuc. Sci.*, **NS-26**, this issue (1979).
9. M. J. Bernstein, *IEEE Trans. Nuc. Sci.*, **NS-24**, 2512 (1977).
10. D. Fromme, V. Van Lint, R. Stettner, and C. Mallon, *IEEE Trans. Nuc. Sci.*, **NS-24**, 2529 (1977).

11. E. Storm and H. I. Israel, "Photon Cross Sections from 0.001 to 100 MeV for Elements 1 through 100," LA-3753, Los Alamos Scientific Laboratory, New Mexico (1967).
12. J. H. Hubbell, Atomic Data, 3, 241 (1971).
13. F. Biggs and R. Lighthill, "Analytical Approximations for X-ray Cross Sections II," SC-RR-71-0507, Weapons Effects Research Department, Sandia Laboratories, Albuquerque, New Mexico (1971).
14. S. T. Manson and J. C. Cooper, Phys. Rev. 165, 126 (1968).
15. E. J. McGuire, "Atomic Subshell Photoionization Cross Sections for  $2 \leq Z \leq 54$ ," SC-RR-70-721, Sandia Laboratories, New Mexico (1970).
16. D. L. Lin and D. J. Strickland, "Photoionization, Electron Impact Inverse Mean Free Paths, and Stopping Power for Each Subshell of Ag," SAL-102-78-22, to be published.
17. Handbook of Auger Electron Spectroscopy, Physics Electronics Industries, Inc. (1976).
18. D. L. Lin, B. L. Beers, and D. J. Strickland, IEEE Trans. Nuc. Sci., NS-25, No. 6, 1561 (1978).
19. C. J. Tung, R. H. Ritchie, J. C. Ashley, and V. E. Anderson, "Inelastic Interactions of Swift Electrons in Solids," ORNL-TM-5188, Oak Ridge National Laboratory, Tennessee (1976).
20. J. C. Ashley, C. J. Tung, R. H. Ritchie, and V. E. Anderson, "Inverse Mean Free Path, Stopping Power, CSDA Range, and Straggling in Polystyrene for Electrons of Energy  $\leq 10$  keV," RADC-TR-78-32 (1978).
21. P. W. Palmberg and T. M. Rhodin, J. Appl. Phys. 39, 2425 (1968).
22. D. C. Jackson, T. E. Gallon, and A. Chambers, Sur. Sci. 36, 381 (1973).
23. C. J. Powell, Sur. Sci. 44, 29 (1974).

TABLE 1. BINDING ENERGIES AND AUGER FEATURES OF Ag

BINDING ENERGIES OF Ag

SHELLS	BINDING ENERGY (keV)
K	24.7
L	3.35
M <sub>1</sub>	0.665
M <sub>23</sub>	0.567
M <sub>45</sub>	0.384
N	0.0127

AUGER FEATURES OF Ag

TRANSITION	ENERGY (keV)	YIELD
KLL	18.8	0.166
LMM	2.57	0.900
MNN	0.355	1.000

TABLE 2. BINDING ENERGIES AND AUGER FEATURES OF C

BINDING ENERGIES

SHELLS	BINDING ENERGIES (keV)
K	0.284
L	0.008

AUGER FEATURES

TRANSITION	ENERGY (keV)	YIELD
KLL	0.272	1.00

TABLE 3. EWR PHOTOEMISSION YIELDS IN  $10^{-5}$  coul/cal

MATERIAL	THIS WORK	BERNSTEIN	FROMME, ET AL.
Al	1.5		
Al <sub>2</sub> O <sub>3</sub>	0.82	1.3	1.8
Au	3.2	2.1	2.1
Ag	0.88	1.5	1.6
C	0.21	0.20	0.16

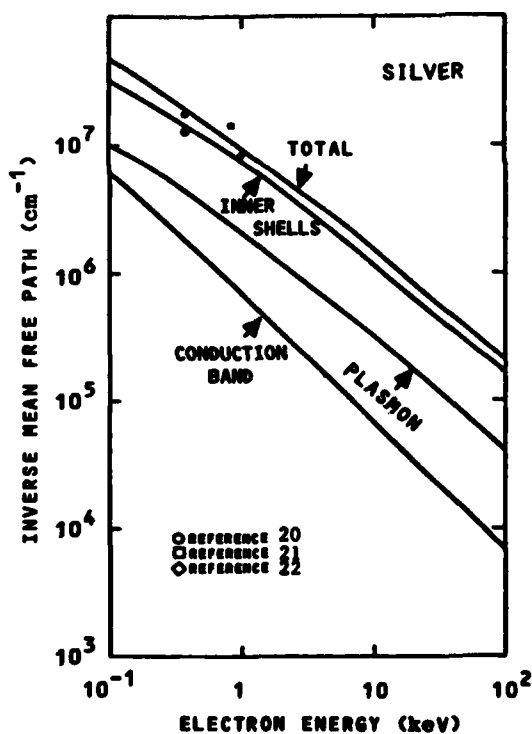


FIGURE 1. INELASTIC INVERSE MEAN FREE PATHS OF Ag.

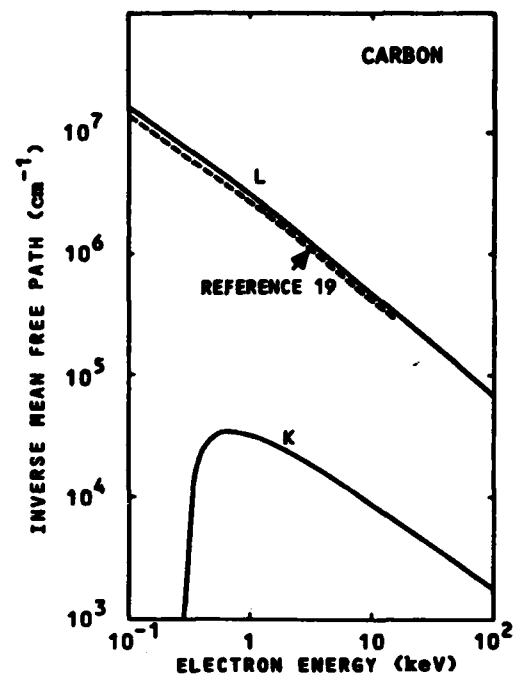


FIGURE 2. INNER SHELL INVERSE MEAN FREE PATHS OF C.

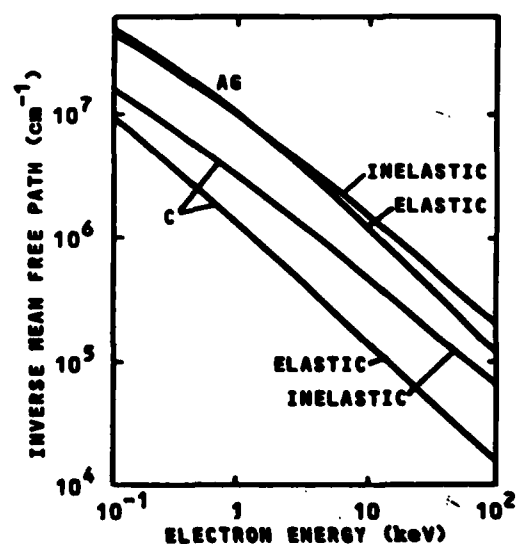


FIGURE 3. TOTAL INELASTIC AND ELASTIC INVERSE MEAN FREE PATHS OF Ag AND C.

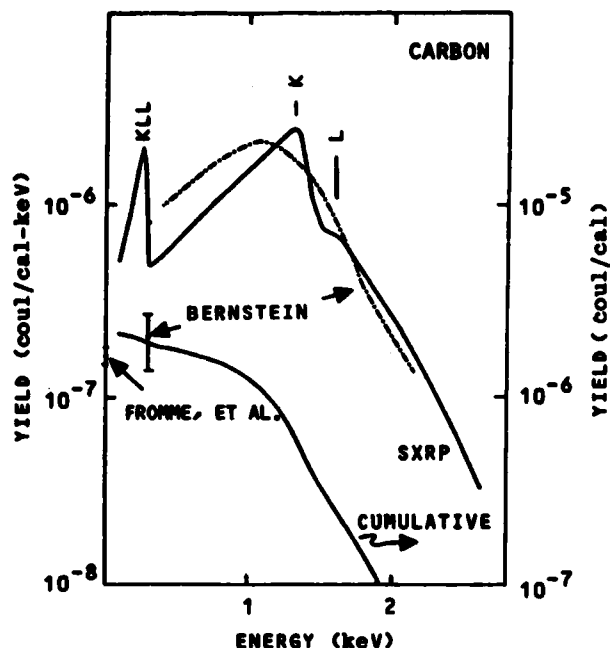


FIGURE 4. CALCULATED AND MEASURED PHOTOEMISSION SPECTRUM AND ITS CUMULATIVE BACK YIELD FOR AN EMR SOURCE INCIDENT ON C.

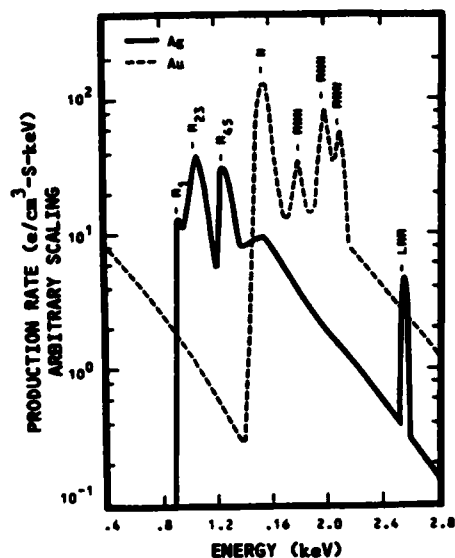


FIGURE 6. ELECTRON SOURCE SPECTRA FOR EMR X-RAY SOURCE INCIDENT ON Ag AND Au.

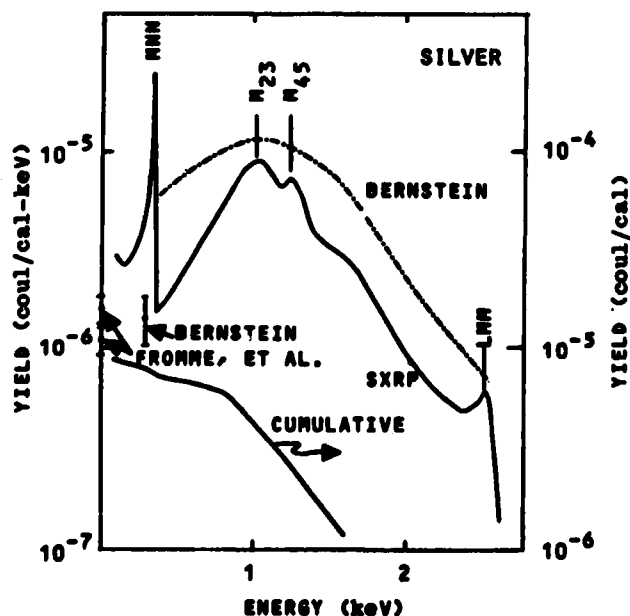


FIGURE 5. CALCULATED AND MEASURED PHOTOEMISSION SPECTRUM AND CUMULATIVE BACK YIELD FOR AN EMR SOURCE INCIDENT ON Ag.

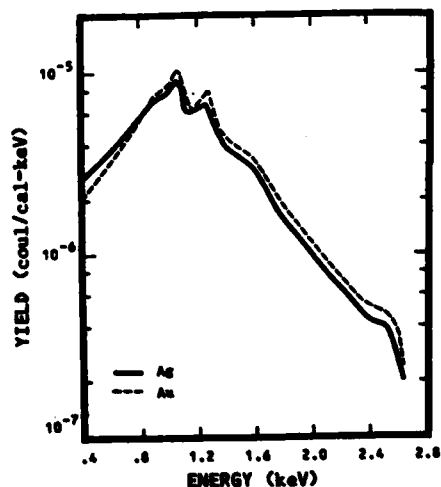


FIGURE 7. PHOTOEMISSION SPECTRA FROM Ag AND Au FOR THE SAME ELECTRON SOURCE SPECTRUM, NAMELY THAT OF Ag SHOWN IN FIGURE 6.

**APPENDIX C**

# Photoionization cross sections, electron-impact inverse mean free paths, and stopping powers for each subshell of silver <sup>a)</sup>

D. L. Lin and D. J. Strickland

Radiation and Electromagnetics Division, Science Applications, Inc., 8330 Old Courthouse Road, Vienna, Virginia 22180

(Received 3 August 1979; accepted for publication 29 October 1979)

Using the Herman-Skillman potentials and bound wave functions for each subshell of silver, we have computed the continuum wave functions, and subshell-by-subshell photoionization cross sections with photoelectron energies up to 10 keV. Applying a relationship between photoionization and electron impact ionization, we have obtained inverse mean free paths and stopping powers, again by subshell, for electrons penetrating through silver. The maximum electron energy considered is 100 keV. For the total photoionization cross section, comparison of our work with experiment shows excellent agreement for photon energies down to 100 eV, below which solid-state effects should be included. Theoretical total inverse mean free paths, being strongly dominated by contributions from 4d electrons, are in good agreement with data around 1 keV, but about a factor of 2 larger at energies below 100 eV. Our stopping power is in good agreement with other theoretical work above 400 eV and approaches the relativistic Bethe formula above 10 keV. Range is also computed and is in good agreement with other theoretical work.

PACS numbers: 32.80.Fb, 34.80.Dp, 79.20.Kz

## I. INTRODUCTION

Interest in photon attenuation in materials dates back to the beginning of this century. The information about attenuation coefficients is frequently needed for the analysis of radiation experiments and for application to medical, engineering, crystallographic, and other practical problems.

Most recently, soft x-ray photoemission and electron transport studies for radiation hardening of devices<sup>1</sup> requires detailed subshell-by-subshell information about photoabsorption coefficients and inverse mean free paths (IMFP's) of electron-impact ionization. Another area of interest is surface physics. A technique, called electron spectroscopy for chemical analysis (ESCA), was developed in the late 1960's in which an x-ray beam is directed onto a solid specimen and photoelectrons are collected and their energies analyzed. Closely related to ESCA is Auger electron spectroscopy (AES) in which an electron beam is incident on a specimen and Auger electrons are collected. Interpretation of these spectral measurements also requires the above type of detailed information.

In studying the penetration of charged particles into materials, Bethe<sup>2</sup> developed a simple stopping power formula applicable to high-energy incident particles. In the intermediate energy region, the stopping power calculated from the atomic picture is presumably adequate. It is generally assumed that for electron energies below roughly 100 eV, solid-state effects will play a dominant role for stopping. Recently, calculations were made<sup>3</sup> for the inverse mean free paths and stopping power due to conduction band ionization and plasmon excitation for various materials using the method of the dielectric response function. In this paper, we try to assess how low in energy the atomic picture can be applied in

the calculation of subshell-by-subshell IMFP's and the stopping power, what the dominant contribution is, and, furthermore, what kind of solid-state picture we should take in improving our atomic calculations at low energies. In Sec. II, we will briefly describe the theory of photoionization and a relationship between the photoionization and electron-impact ionization. Section III discusses the numerical approach. Results and comparison will be made in Sec. IV.

## II. THEORY

The transition rate for the photoionization process in which the incident photon is absorbed and an atomic electron is ejected can be obtained from quantum theory. Briefly, a  $\delta$ -normalized continuum state with momentum  $k$  (the final state) can be expanded in terms of spherical harmonics and radial wave functions. Integrating over all directions of  $k$  and using the asymptotic behavior of the radial wave function, one can prove that the transition rate is given by (we use atomic units):

$$R = 2\pi |\langle \psi_{k,l} | H_{int} | \psi_i \rangle|^2. \quad (1)$$

The continuum radial wave function  $R_{k,l}$  of  $\psi_{k,l}$  has the well-known asymptotic form

$$\left(\frac{2}{\pi k}\right)^{1/2} \frac{1}{r} \sin[\phi(r) + \delta_l],$$

$l$ , being the angular momentum of the final electron and  $H_{int}$  the interaction Hamiltonian.  $\psi_i$  refers to the initial wave function. Dividing the transition rate by the incident photon flux, the photoionization cross section is obtained:

$$\sigma(\omega, l_f) = \frac{4\pi^2 \alpha}{\omega} |\langle \psi_{k,l_f} | \mathbf{p} \cdot \mathbf{e} | \psi_i \rangle|^2. \quad (2)$$

$\alpha$  is the fine-structure constant and  $\omega$  is the angular frequency of the photon. The evaluation of the angular part in the above matrix element can be done by the technique of re-

<sup>a)</sup>Work supported in part by Defense Nuclear Agency.

duced matrix elements. In the independent particle approximation, the cross section reduces to

$$\sigma_{\text{length}} = \frac{4\pi^2\alpha}{3} \frac{N_{nl} l_{\text{max}}}{2l_i + 1} \omega \left( \int P_{nl} r P_{kl} dr \right)^2, \quad (3)$$

$$\sigma_{\text{velocity}} = \frac{4\pi^2\alpha}{3} \frac{N_{nl} l_{\text{max}}}{2l_i + 1} \omega \times \left[ \frac{-1}{\omega} \int P_{nl} \left( \frac{d}{dr} + \frac{(l_f - l_i)(l_f + l_i + 1)}{2r} \right) P_{kl} dr \right]^2 \quad (4)$$

for length and velocity forms, respectively. In these expressions,  $N_{nl}$  refers to the number of electrons in the initial subshell  $nl$ .  $l_{\text{max}}$  is the maximum value of  $l$ , and  $l_f$ ,  $P_{nl} \equiv rR_{nl}$ , and  $P_{kl} \equiv rR_{kl}$ . For radial wave functions in any local potential, these two cross sections will yield identical results.

The differential equation satisfied by the continuum wave function  $P_{kl}$  is given by

$$\left( \frac{d^2}{dr^2} + V(r) + k^2 - \frac{l(l+1)}{r^2} \right) P_{kl}(r) = 0. \quad (5)$$

Once the subshell photoionization cross sections are known, the corresponding electron-impact ionization cross sections and hence IMPF's can be obtained by an approximate method recently developed by us.<sup>4</sup> The formula we obtain is given in atomic units by

$$K(E_i) = \int_B^{E_i} \frac{dK(E_i, \epsilon)}{d\epsilon} d\epsilon, \\ = \frac{1}{\pi\alpha E_i} \int_B^{E_i} \left( \frac{a_\gamma(\epsilon)}{\epsilon} \right) \ln \frac{q_{\text{max}}}{q_{\text{min}}} d\epsilon, \quad (6)$$

where  $K$  is the IMPF's,  $E_i$  represents the energy of the incident electron,  $B$  is the binding energy of the subshell in question, and  $a_\gamma(\epsilon)$  denotes the photoabsorption coefficient for photon energy.  $q_{\text{max}}$  and  $q_{\text{min}}$  are momentum transfers:

$$q_{\text{max}}^2 = 2E_i + 2(E_i - \epsilon) - 2(2E_i)^{1/2} [2(E_i + B - 2\epsilon)]^{1/2}, \quad (7)$$

$$q_{\text{min}}^2 = 2E_i + 2(E_i - \epsilon) - 2(2E_i)^{1/2} [2(E_i - \epsilon)]^{1/2}. \quad (8)$$

From the subshell IMPF's, one can compute, in atomic units, the corresponding stopping powers

$$S(E_i) = \int_0^{(E_i + B)^{1/2}} \epsilon \frac{dK(E_i, \epsilon)}{d\epsilon} d\epsilon, \quad (9)$$

and ranges

$$R(E) = \int_{E_0}^E \frac{dE'}{S(E')}. \quad (10)$$

We choose  $E_0 = 0.37$ , corresponding to 10 eV.

### III. NUMERICAL APPROACH

To solve Eq. (5), we adopt an approach quite similar to that of Cooper<sup>5</sup> and Manson and Cooper.<sup>6</sup> The formulas for the Runge-Kutta method are obtained from Hildebrand,<sup>7</sup> slightly different from Refs. 5 and 6. The continuum wave function  $P_{kl}(r)$  near the origin is obtained from Hartree.<sup>8</sup> Bound wave functions, central potentials, and binding energies are tabulated in the literature.<sup>9</sup> The phase shift was com-

puted following the method suggested by Sauton and Peach.<sup>10</sup> The normalization constant can be calculated by a simple extension of this method, as given in the appendix of Ref. 5. The two points chosen in the present work for the calculation of the normalization constant are usually separated by a few wavelengths rather than neighboring grid points, as adopted by others. To assure that the correct normalization constant was obtained, we calculated it for a few different pairs of points. Since we are interested in cases where the energies of the photoelectron range from a few eV to 10 keV, the iterative scheme is adopted in solving the nonlinear equation for the amplitude of the continuum radial wave function, instead of the first order iteration approximation as used in Refs. 5 and 6. The iteration is stopped when the absolute fractional changes of the quantity in question at all points considered are less than 0.0005. Usually two iterations are needed for  $s, p, d$ , and  $f$  photoelectrons of silver.

Calculations of the photoionization cross sections of bound electrons of a given angular momentum, but different principal quantum numbers, were carried out in one run. To treat the wide ranges in photoelectron energies and binding energies (hence, bound wave functions), we chose to have 20 radial grid points within a quarter wavelength of the photoelectron wave function and, at the same time, allowed for at least 200 grid points within the maximal radius of the most tightly bound electron. Uniform grid size was doubled every 40 grid points. The calculation of the continuum wave function starts at a radius where the fractional change

$$[\zeta^2(x) - \zeta^2(x)]/\zeta^2(x)$$

becomes smaller than one-thousandth [ $\zeta^2(s)$  being the inverse of the amplitude of the radial wave function].

### IV. RESULTS AND DISCUSSION

The subshell photoionization cross sections of silver

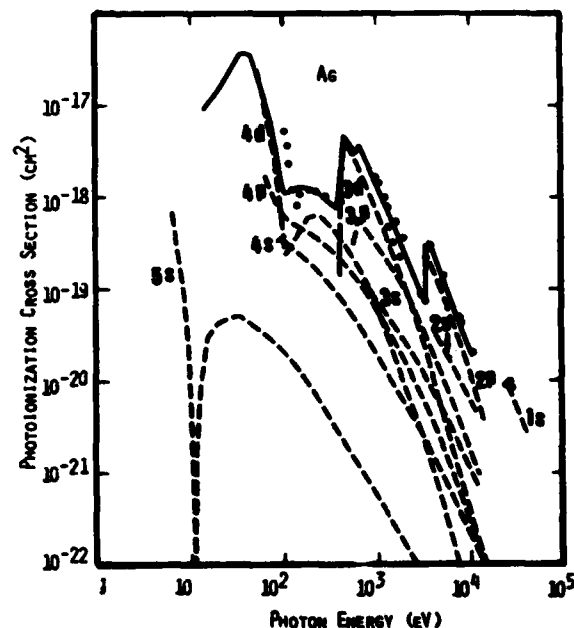


FIG. 1. Subshell photoionization cross sections of Ag.

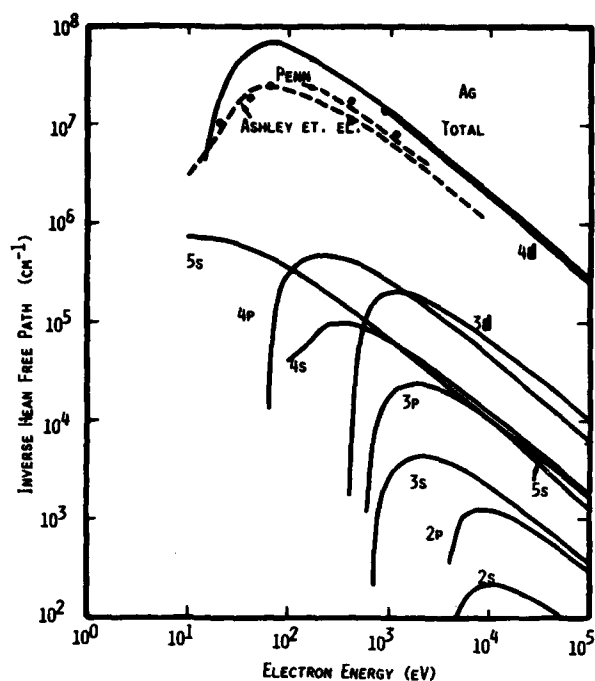


FIG. 2. Inverse mean free paths of electrons incident on Ag. Results of two other theoretical calculations (Refs. 15 and 16) are also shown. See Ref. 15 for data references.

calculated from the method described above are shown as dashed curves in Fig. 1. The solid curve represents the total cross section. The data points are taken from the data compilation of Hubbell.<sup>11</sup>

The transition matrix elements of Eqs. (3) and (4) change sign for the case of 5s electron when the photon energy passes through  $\sim 11$  eV. This is the so-called "Cooper

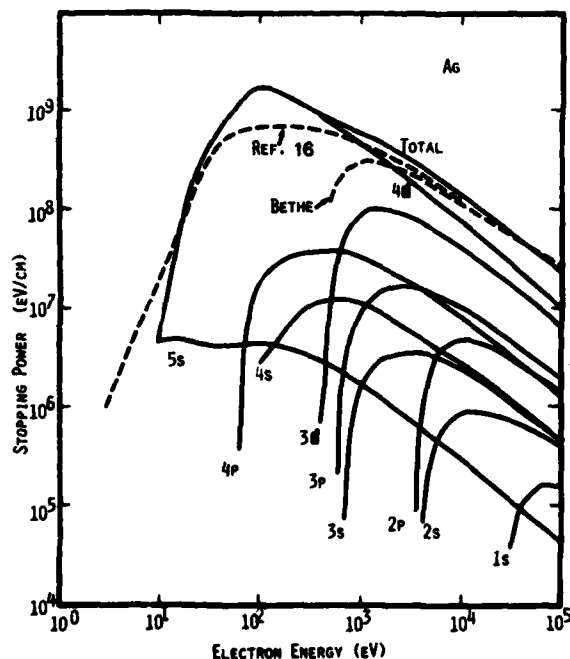


FIG. 3. Stopping power for each subshell of Ag.

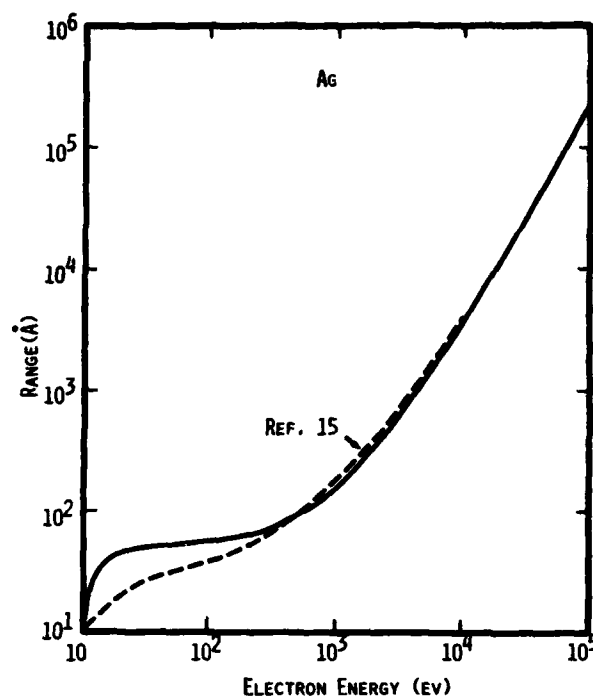


FIG. 4. Range of electrons in Ag. Minimum electron energy is 10 eV.

minimum"<sup>12</sup> where the photoabsorption coefficient of a particular bound electron becomes zero. The structure of the total cross section curve between 100 and 300 eV is due mainly to the contributions from 4p and 4d electrons. The 5s electron does not have any significant photoionization cross section in the energy range shown.

The agreement between our atomic calculation and the experimental data of solid silver is excellent in the soft x-ray range of 100 eV to 30 keV. Below 100 eV, we do not anticipate good qualitative agreement between our calculations and experiments due to the neglect of the solid-state effects, which include the formation of the band structure and shifting of the atomic energy levels,<sup>13</sup> and the correlation effects between electrons. Qualitatively, Fig. 1 indicates the contribution at low energies comes mainly from 4d electrons. For example, at the photon energy  $\sim 40$  eV, the transition matrix element of the 4d electron is about two orders of magnitude larger than that of 5s. Assuming no significant change in the subshell photoionization cross section in going from an atomic picture to a solid-state picture the 4d band will be responsible for most of the observed photoabsorption coefficient at energies below 100 eV.

We have also calculated the subshell photoionization cross sections using a screened hydrogenic model.<sup>14</sup> This model is reliable for the most tightly bound K-shell electrons, but gets worse as the principal quantum number increases. For example, using a screening parameter of 10.13 for the 3s electron of silver, we found the photoionization cross section to be about a factor of 2 larger than that of the present approach.

Relativistic effects neglected in the present calculation of photoionization cross section are not important, as is evi-



dent when comparison is made with Scofield's relativistic calculation<sup>15</sup> of Hartree-Slater subshell photoionization cross sections at 1254 and 1487 eV. Agreement is better than 5% for any subshell of silver.

Figure 2 shows the subshell inverse mean free paths for incident electrons with energies ~ 10 eV to 100 keV. Total IMFP's and data points are also shown in Fig. 2. Our total IMFP is seen to be about a factor of 2 larger than the data above a few hundred eV and a factor of 3 larger at lower energies. As far as individual subshell contributions are concerned, the 4d subshell dominates. Since we do not expect good agreement between the atomic photoionization curve and solid-state photoabsorption data at lower energies (tens of eV), the results computed from Eq. (6) using this atomic curve will not correspond exactly to the solid-state IMFP data. Judging from this consideration, the fair agreement mentioned above is viewed as satisfactory.

The results of a statistical model, computed by Ashley *et al.*<sup>16</sup> and shown in Fig. 2, agree with the data at tens of eV. At hundreds of eV, our curve is on the upper side, whereas that of the statistical model is on the lower side of the data. From 1 to 10 keV, these two theoretical curves, based upon quite different approaches, do agree within a factor of 2.

Penn<sup>17</sup> has carried out calculations of the total IMFP, again using the method of the dielectric response function, for elements up to  $Z = 83$ . The energy range is between 200 and 2400 eV. For silver, his results are also plotted in Fig. 2. Being based on the same approach, this curve is quite similar to that of Ashley *et al.*

Our subshell IMFP curves can be employed in Eq. (9) to generate subshell stopping powers for incident electrons with energies from 10 eV to 100 keV. Figure 3 shows our results. The 4d subshell dominates at energies below 1 keV. However, the 3d subshell becomes comparably important for higher energies, due to the large binding energy of the bound 3d electrons.

The stopping power computable from the statistical model is in good agreement with our total result, as shown in Fig. 3. In fact, they are within about 20% of each other for incident electron energies from 1 to 10 keV. We have also included the stopping power computed from the relativistic Bethe formula<sup>18</sup>:

$$-\frac{dE}{dx} = \frac{2\pi Ne^4}{mv^2} Z \left[ \log \left( \frac{mv^2 E}{2I^2(1-\beta^2)} \right) - [2(1-\beta^2)^{1/2} + 1 + \beta^2] \log 2 + 1 - \beta^2 + \frac{1}{2} [1 - (1-\beta^2)^{1/2}]^2 \right], \quad (11)$$

where  $I$ , a weighted average of the excitation and ionization potentials of the atom of the stopping material, is taken from the semiempirical formula<sup>19</sup>

$$I = 9.1Z(1 + 1.9Z^{-2/3}) \text{ eV}. \quad (12)$$

Our total stopping power is in good agreement with the Bethe formula at high energies for which the latter is applicable. The cross-over energy of these two stopping curves is at ~ 50 keV.

The range, as defined by Eq. (10), was also calculated and is shown in Fig. 4. For comparison, we also include the range curve from the statistical model.<sup>16</sup> The agreement of

these curves is reasonably good between 100 eV and 10 keV with the crossover energy at ~ 400 eV. The relatively sharp rise of our range near 10 eV is due to the small stopping power there.

## V. CONCLUSION

Using an atomic description, we have computed *ab initio*, the subshell photoionization cross sections followed by inverse mean free paths and stopping powers of silver. A range calculation was also carried out using our results for the total stopping power. Theoretical curves for total quantities were compared with available solid-state experimental data, as well as other theoretical results. Generally good agreement is found for energies (of either photon or incident electron) above 100 eV. Below this energy, where solid-state effects as well as correlation effects become important, the agreement is still fair. By separating the total curve of a given observable quantity into contributions from individual subshell, we are able to assess the relative importance of each subshell in treating solid-state effects or correlation effects. For example, we find that the 4d band of silver should be modeled in greater detail in the solid state.

Even though other theoretical works calculating subshell contributions to a given observable are not available<sup>20</sup> for comparison, we believe that our results for individual inner shell contributions are quite accurate based on the observation that our photoionization cross sections are in excellent agreement with data for the inner shells.

<sup>1</sup>D.J. Strickland, IEEE Trans. Nucl. Sci. NS-24, 2499 (1977); D.J. Strickland, D.L. Book, T.P. Coffey, and J.A. Fedder, J. Geophys. Res. 81, 2755 (1976).

<sup>2</sup>H.A. Bethe, Ann. Phys. 5, 325 (1930); H.A. Bethe and J. Ashkin, *Experimental Nuclear Physics*, edited by E. Segre (Wiley, New York, 1953), Vol. 1.

<sup>3</sup>J.C. Ashley, C.J. Tung, and R.H. Ritchie, IEEE Trans. Nucl. Sci. NS-22, 2533 (1975); C.J. Tung and R.H. Ritchie, Phys. Rev. B 16 4302 (1977); J.C. Ashley, C.J. Tung, and R.H. Ritchie, IEEE Trans. Nucl. Sci. NS-25, 1566 (1978).

<sup>4</sup>D.L. Lin, B.L. Beers, and D.J. Strickland, IEEE Trans. Nucl. Sci. NS-25, 1561 (1978). The basic theory was derived long ago; see Ref. 2; Chap. XVI of N.F. Mott and H.S.W. Massey, *Theory of Atomic Collisions* (Oxford U.P., London, 1965), Chap. XVI; M. Inokuti, Rev. Mod. Phys. 43, 297 (1977). The main difference in our work is the consideration of the maximum cutoff momentum.

<sup>5</sup>J.W. Cooper, Phys. Rev. 128, 681 (1962).

<sup>6</sup>S.T. Manson and J.W. Cooper, Phys. Rev. 165, 126 (1968).

<sup>7</sup>F.B. Hildebrand, *Introduction to Numerical Analysis*, 2nd ed., (McGraw-Hill, New York, 1974) pp. 291 and 292.

<sup>8</sup>D.R. Hartree, *The Calculations of Atomic Structure*, (Wiley, New York, 1957).

<sup>9</sup>F. Herman and S. Skillman, *Atomic Structure Calculations* (Prentice-Hall, Inc., Englewood Cliffs, N.J., 1963).

<sup>10</sup>M.J. Seaton and G. Peach, Proc. Phys. Soc. London 79, 1296 (1962).

<sup>11</sup>J.H. Hubell, At. Data 3, 241 (1971).

<sup>12</sup>J.W. Cooper, Phys. Rev. Lett. 13, 762 (1964).

<sup>13</sup>An example of this LiF crystal is given by A.B. Kunz, D.J. Mickish, and T.C. Collins [Phys. Rev. Lett. 31, 756 (1973)].

<sup>14</sup>J.M. Harriman, Phys. Rev. 101, 594 (1956).

<sup>15</sup>J.H. Scofield, J. Electron Spectrosc. Related Phen. 8, 129 (1976).

<sup>16</sup>J.C. Ashley, C.J. Tung, R.H. Ritchie, and V.E. Anderson, Oak Ridge National Laboratory Health Phys. Div. Report RADC-TR-76-220, 1976.

<sup>17</sup>D.R. Penn, J. Electron Spectrosc. Related Phen 9, 29 (1976).

<sup>18</sup>H.A. Bethe and J. Ashkin, *Experimental Nuclear Physics*, edited by E. Segre (Wiley, New York, 1953), Vol. 1.

<sup>19</sup>E. Segre, *Nuclei and Particles* (Benjamin, New York, 1964).

<sup>20</sup>The semi-empirical Lotz formula [W. Lotz, Z. Phys. 206, 205 (1967); 216, 241 (1968)] is only applicable to  $Z \leq 20$ .

## DISTRIBUTION LIST

### DEPARTMENT OF DEFENSE

Assistant to the Secretary of Defense  
Atomic Energy  
ATTN: Executive Assistant

Defense Intelligence Agency  
ATTN: DB-4C

Defense Nuclear Agency  
2 cy ATTN: RAEV  
4 cy ATTN: TITL

Defense Technical Information Center  
12 cy ATTN: DD

Field Command  
Defense Nuclear Agency  
ATTN: FCPR  
ATTN: FCLMC

Field Command  
Defense Nuclear Agency  
Livermore Division  
ATTN: FCPRL

Interservice Nuclear Weapons School  
ATTN: TTV

Joint Chiefs of Staff  
ATTN: J-5, Nuclear Division  
ATTN: C3S Evaluation Office

Joint Strat. Tgt. Planning Staff  
ATTN: JLTW-2  
ATTN: JLA

National Communications System  
ATTN: NCS-TS

Undersecretary of Defense for Rsch. & Engrg.  
ATTN: Strategic & Space Systems (OS)

### DEPARTMENT OF THE ARMY

BMD Advanced Technology Center  
Department of the Army  
ATTN: ATC-O

BMD Systems Command  
Department of the Army  
ATTN: BDMSC-H

Deputy Chief of Staff for Rsch. Dev. & Acq.  
Department of the Army  
ATTN: DAMA-CSS-N

Electronics Tech. & Devices Lab.  
U.S. Army Electronics R&D Command  
ATTN: DRSEL

Harry Diamond Laboratories  
Department of the Army  
ATTN: DELHD-N-RBC, R. Gilbert  
ATTN: DELHD-I-TL

U.S. Army Communications Sys. Agency  
ATTN: CCM-AD-LB

### DEPARTMENT OF THE ARMY (Continued)

U.S. Army Foreign Science & Tech. Ctr.  
ATTN: DRXST-IS-1

U.S. Army Missile R&D Command  
ATTN: RSIC

### DEPARTMENT OF THE NAVY

Naval Research Laboratory  
ATTN: Code 6701  
ATTN: Code 7550, J. Davis  
ATTN: Code 6707, K. Whitney

Naval Surface Weapons Center  
ATTN: Code F31

Strategic Systems Project Office  
Department of the Navy  
ATTN: NSP

### DEPARTMENT OF THE AIR FORCE

Air Force Geophysics Laboratory  
ATTN: PH, C. Pike

Air Force Weapons Laboratory  
Air Force Systems Command  
ATTN: SUL  
ATTN: NT  
ATTN: NXS  
2 cy ATTN: DYC

Ballistic Missile Office  
Air Force Systems Command  
ATTN: MNRT  
ATTN: MNG  
ATTN: MNNH

Deputy Chief of Staff  
Research, Development, & Acq.  
Department of the Air Force  
ATTN: AFRDQSM

Headquarters Space Division  
Air Force Systems Command  
ATTN: SKF

Rome Air Development Center  
Air Force Systems Command  
ATTN: ESR, E. Burke

Strategic Air Command  
Department of the Air Force  
ATTN: NRI-STINFO Library  
ATTN: XPFS

### OTHER GOVERNMENT AGENCY

NASA  
Lewis Research Center  
ATTN: N. Stevens  
ATTN: C. Purvis  
ATTN: Library

DEPARTMENT OF ENERGY CONTRACTORS

Lawrence Livermore National Laboratory  
ATTN: Technical Information Dept. Library

Los Alamos National Scientific Laboratory  
ATTN: MS 364

Sandia National Laboratories  
Livermore Laboratory  
ATTN: T. Dellin

Sandia National Laboratories  
ATTN: 3141

DEPARTMENT OF DEFENSE CONTRACTORS

Aerospace Corp.  
ATTN: V. Josephson  
ATTN: J. Reinheimer  
ATTN: Library

AVCO Research & Systems Group  
ATTN: Library, A830

Boeing Co.  
ATTN: P. Geren

Computer Sciences Corp.  
ATTN: A. Schiff

Dikewood Industries, Inc.  
ATTN: Technical Library

Dikewood Industries, Inc.  
ATTN: K. Lee

EG&G Washington Analytical Services Center, Inc.  
ATTN: Library

Eugene P. DePlomb  
ATTN: E. DePlomb

Ford Aerospace & Communications Corp.  
ATTN: A. Lewis  
ATTN: Technical Library

General Electric Co.  
ATTN: J. Peden

General Electric Company-TEMPO  
ATTN: DASIAC  
ATTN: W. McNamara

Hughes Aircraft Co.  
ATTN: Technical Library

Hughes Aircraft Co.  
ATTN: E. Smith  
ATTN: W. Scott  
ATTN: A. Narevsky

Institute for Defense Analyses  
ATTN: Classified Library

DEPARTMENT OF DEFENSE CONTRACTORS (Continued)

IRT Corp.  
ATTN: Library  
ATTN: D. Swift  
ATTN: N. Rudie

JAYCOR  
ATTN: E. Wenaas  
ATTN: Library

JAYCOR  
ATTN: R. Sullivan

Johns Hopkins University  
ATTN: P. Partridge

Kaman Sciences Corp.  
ATTN: W. Rich  
ATTN: Library  
ATTN: J. Lubell

Lockheed Missiles & Space Co., Inc.  
ATTN: DEPT. 85-85

McDonnell Douglas Corp.  
ATTN: S. Schneider

Mission Research Corp.  
ATTN: C. Longmire  
ATTN: R. Stettner

Mission Research Corporation-San Diego  
ATTN: V. Van Lint  
ATTN: Library

R & D Associates  
ATTN: C. MacDonald  
ATTN: Technical Information Center  
ATTN: L. Schlessinger  
ATTN: P. Haas

Rockwell International Corp.  
ATTN: Library

Science Applications, Inc.  
ATTN: W. Chadsey  
ATTN: D. Lin

Spire Corp.  
ATTN: R. Little

SRI International  
ATTN: Library

Systems, Science & Software, Inc.  
ATTN: A. Wilson  
ATTN: Library

TRW Defense & Space Sys. Group  
ATTN: E. Chivington  
ATTN: Technical Information Center